

High-performance magnesium/sodium hybrid ion battery based on sodium vanadate oxide for reversible storage of Na⁺ and Mg²⁺

Xiaoke Wang^{a,b,c}, Titi Li^b, Xixi Zhang^b, Yaxin Wang^c, Hongfei Li^c, Hai-Feng Li^{a,*},
Gang Zhao^{b,*}, Cuiping Han^{d,*}

^a *Institute of Applied Physics and Materials Engineering, University of Macau, Avenida da Universidade, Taipa, Macao SAR, 999078, China*

^b *School of Physics and Technology, University of Jinan, Shandong 250022, PR China*

^c *Songshan Lake Materials Laboratory, Dongguan, Guangdong, 523808, China*

^d *Faculty of Materials Science and Energy Engineering / Institute of Technology for Carbon Neutrality, Shenzhen Institute of Advanced Technology, Chinese Academy of Sciences, Shenzhen, Guangdong, 518055, China*

* Corresponding authors.

E-mail addresses: haifengli@um.edu.mo (H.-F. Li), sps_zhaog@ujn.edu.cn (G. Zhao), cp.han@siat.ac.cn (C.P. Han).

ABSTRACT

Magnesium ion batteries (MIBs) are a potential field for the energy storage of the future but are restricted by insufficient rate capability and rapid capacity degradation. Magnesium-sodium hybrid ion batteries (MSHBs) are an effective way to address these problems. Here, we report a new type of MSHBs that use layered sodium vanadate ((Na, Mn)V₈O₂₀·5H₂O, Mn-NVO) cathodes coupled with an organic 3,4,9,10-perylenetetracarboxylic diimide (PTCDI) anode in Mg²⁺/Na⁺ hybrid electrolytes. During electrochemical cycling, Mg²⁺ and Na⁺ co-participate in the cathode reactions, and the introduction of Na⁺ promotes the structural stability of the

Mn-NVO cathode, as cleared by several *ex-situ* characterizations. Consequently, the Mn-NVO cathode presents great specific capacity (249.9 mAh g⁻¹ at 300 mA g⁻¹) and cycling (1500 cycles at 1500 mA g⁻¹) in the Mg²⁺/Na⁺ hybrid electrolytes. Besides, full battery displays long lifespan with 10,000 cycles at 1000 mA g⁻¹. The rate performance and cycling stability of MSHBs have been improved by an economical and scalable method, and the mechanism for these improvements was discussed.

Keywords: Aqueous battery; Hybrid ion battery; Mg²⁺/Na⁺ co-intercalation; High-rate performance; Organic-water hybrid electrolyte

1. Introduction

Rechargeable magnesium ion batteries (MIBs) are favorable electrochemical energy storage systems that can meet future electrical energy storage requirements[1,2] due to their potential advantages, such as the large theoretical volumetric capacity of magnesium (3833 mAh cm⁻³) and minimal environmental impact[2,3]. Magnesium resources are abundant, evenly distributed, easy to mine on earth, and have an inherent cost advantage[4,5]. Nevertheless, due to their small ionic radius as well as multi-electron redox reactions, metal cations like Mg²⁺ exhibit a high charge density (0.72 Å for Mg²⁺, 0.76 Å for Li⁺)[6,7]. The high charge density of Mg²⁺ leads to sluggish solid-state diffusion, resulting in strong polarization and low intercalation efficiency in electrode materials[8,9]. Despite considerable effort, these reversibility advances are mostly achieved at a slower rate (< 0.5 C)[10]. Therefore, MIBs suffer from insufficient cycling and rate performance[11]. It remains an obvious challenge

for MIBs to obtain excellent performance in practical applications[12,13].

To date, a variety of tactics have been pursued thus far to raise the cycling stability and rate capability of MIBs[14], containing interface engineering of magnesium anodes[15], electrode material structure modification[9], electrolyte regulation[2], capacity-compensation has emerged from the dynamic redox of copper ions [16], and so on. A suitable solution is to add alien cations (e.g., Li^+ , Na^+) for better kinetic performance. Such batteries can be called magnesium-lithium/sodium hybrid ion batteries (MLHBs, MSHBs)[17]. Previously, an efficient method to address this issue is to build MLHBs that benefit from a dendrite-free magnesium anode and accelerated Li^+ kinetics facilitated by a dual-salt electrolyte that contains Mg^{2+} and Li^+ ions[18,19]. Compared with MLHBs, MSHBs have been relatively less studied and, the obtained cycle stability or specific capacity in MSHBs remains unsatisfactory[20]. As shown in Table S1, a type of sulfides and oxides cathode, such as FeS_2 [21], $\text{Na}_2\text{VTi}(\text{PO}_4)_3$ [22], Mn_3O_4 [23], $\text{Mg}_{1.5}\text{VCr}(\text{PO}_4)_3$ [20] and $\text{FeFe}(\text{CN})_6$ [24] has been prepared in the MSHBs. However, some of the cathode materials have limited cycle life or insufficient discharge capacity. As a result, there is a pressing demand for cathode materials that exhibit improved performance.

Herein, sodium vanadate oxide ((Na, Mn) $\text{V}_8\text{O}_{20}\cdot 5\text{H}_2\text{O}$, Mn-NVO) materials were proposed as the cathode materials for MSHBs. The Mn-NVO material has an attractive layered structure and the spaces between the metal oxide layers naturally form a two-dimensional diffusion pathway for Mg ion (de)intercalation[25]. Na ions, which possess the advantage of rapid diffusion kinetics, were further introduced

through the utilization of a dual salt electrolyte. The synergistic motion between $\text{Mg}^{2+}/\text{Na}^+$ ions improve the diffusion kinetics, allowing the Mn-NVO cathode to exceptional rate capability and cycling stability. Specifically, Mn-NVO cathode demonstrates notable performance characteristics, including a reversible capacity of 249.9 mAh g^{-1} at 300 mA g^{-1} , enhanced rate performance (130.2 mAh g^{-1} at 300 mA g^{-1}), and durable cyclic performance (1500 cycles at 1500 mA g^{-1} with 88.2% capacity retention), which represents a considerable improvement compared to the up-to-date cathode of MSHBs. *Ex-situ* characterizations have revealed that Mg^{2+} and Na^+ co-participate in the cathode reactions and Mn-NVO cathode endures a reversible phase change throughout the charging and discharging processes. Lastly, the combination of Mn-NVO as the cathode and organic 3,4,9,10-perylenetetracarboxylic diimide (PTCDI) as the anode in a full MSHB, which achieves a remarkable cycle stability of 10,000 cycles at 1000 mA g^{-1} . This work presents a novel excellent performance and high-safe MSHB system that has a large potential for future energy storage applications.

2. Experimental

2.1 Sample preparation

The synthesis of Mn-doped $\text{NaV}_8\text{O}_{20}\cdot 5\text{H}_2\text{O}$ (Mn-NVO) nanobelts was performed using a one-step hydrothermal method. Initially, a mixture of 4.73 g of V_2O_5 (Aladdin, AR, 99%), 1.99 g of Na_2SO_4 (Aladdin, AR, 99%), and 0.676 g of $\text{MnSO}_4\cdot\text{H}_2\text{O}$ (Sinopharma Co., Ltd. Shanghai, China, AR) was dispersed in 50 mL of deionized

water. Subsequently, the pH of the solution was adjusted to 3 by adding CH_3OOH (Aladdin, $\geq 99.8\%$) while stirring on a magnetic stirrer for 30 minutes. The resulting solution was then transferred to a 100 mL Teflon-lined stainless-steel autoclave and heated at 180 °C for 72 hours. Finally, the Mn-NVO samples were dried overnight at 60 °C in a vacuum oven.

2.2 Structural characterizations

X-ray diffraction (XRD) analysis was executed using a D8 Advance X-ray diffractometer (MiniFlex600 with $\text{CuK}\alpha$ radiation) with an angle range from 3 to 90°. X-ray photoelectron spectroscopy (XPS) characterizations were executed using the PHI 5000 VersaProbe II spectrometer equipped with Al $\text{K}\alpha$ radiation. Scanning electron microscopy (SEM) was conducted by scanning electron microscopy (SEM, HITACH S4800, 10kV, 5mA). High-resolution transmission electron microscopy (HR-TEM) and transmission electron microscopy/energy dispersive spectroscopy (TEM-EDS) mapping were conducted using the FEI Tecnai G2 F30 transmission electron microscope (200 kV).

2.3 Electrochemical characterizations

In order to fabricate the cathode, a mixture of the prepared Mn-NVO, Ketjen black, and polyvinylidene fluoride (PVDF) binder was prepared in a weight ratio of 7:2:1. The components were mixed together in N-methyl-2-pyrrolidone (NMP) solvent to form a slurry. This slurry was then coated onto a current collector made of carbon cloth (Ce Tech Co., Ltd). The fabricated electrodes were subsequently dried overnight in a vacuum oven at 60 °C. The electrodes were loaded with active materials at a mass

loading of 1-2 mg cm². In order to fabricate the anode, a mixture of PTCDI, Ketjen black, and polyvinylidene fluoride (PVDF) binder was prepared in a weight ratio of 7:2:1. The components were combined in N-methyl-2-pyrrolidone (NMP) solvent to form a slurry. This slurry was then applied onto a carbon cloth current collector obtained from carbon cloth (Ce Tech Co., Ltd). The resulting electrodes were dried overnight in a vacuum oven at 60 °C. The active materials were loaded onto the electrodes with a mass loading of 4–5 mg cm².

The performance of the prepared Mn-NVO cathode was evaluated electrochemically using three-electrode cells. The Mn-NVO cathode served as the working electrode, a platinum electrode functioned as the counter electrode, and an Ag/AgCl electrode was utilized as the reference electrode. The electrolyte solution was formulated by dissolving 1 M Mg(ClO₄)₂·6H₂O and 1.5 M NaClO₄ in a mixed solvent comprising tetraethylene glycol dimethyl ether (TEGDME) and water, with varying volume ratios (TEGDME: H₂O = 0.8 : 0.2). The 1M Mg(ClO₄)₂·6H₂O dissolved in TEGDME: H₂O = 0.8 : 0.2, 1M Mg(ClO₄)₂·6H₂O + 0.5 M NaClO₄ dissolved in TEGDME: H₂O = 0.8 : 0.2, 1M Mg(ClO₄)₂·6H₂O + 1 M NaClO₄ dissolved in TEGDME: H₂O=0.8:0.2, and 1.5 M NaClO₄ dissolved in TEGDME: H₂O = 0.8 : 0.2 as the controlling electrolyte. Following that, CR-2032 coin cell batteries were fabricated with the Mn-NVO as the cathode and PTCDI as the anode, then 100 μL of 1.5 M NaClO₄ and 1 M Mg(ClO₄)₂ in TEGDME : H₂O = 0.8 : 0.2 electrolytes.

Cyclic voltammetry (CV) of the Mn-NVO cathode, PTCDI anode and the Mn-NVO NVO//PTCDI full cell were performed using an electrochemical station (CHI760E). The scan rates of Mn-NVO cathode ranged from 0.5 to 5 mV s⁻¹, and the voltage range was -0.7 to 1.2 V vs. Ag/AgCl. The scan rates of PTCDI anode employed were 0.1, 0.3, 0.5, 0.8, and 1.0 mV s⁻¹, while the voltage range spanned from -1.1 to 0.2 V vs. Ag/AgCl. The scan rates of the Mn-NVO//PTCDI full battery employed were 1.0, 2.0, 3.0, 4.0, and 5.0 mV s⁻¹, while the voltage range spanned from 0 to 1.8 V. The Mn-NVO cathode, PTCDI anode and Mn-NVO//PTCDI full battery underwent the galvanostatic charge and discharge experiments using a land battery tester (CT2001A). The Mn-NVO cathode at various current densities ranging from 0.3 to 5.0 A g⁻¹. The voltage range for the tests was -0.7 to 1.2 V vs. Ag/AgCl. The PTCDI anode ranging from 0.3 to 5.0 A g⁻¹, The voltage range for the tests was -1.1 to 0.2 V vs. Ag/AgCl. The Mn-NVO//PTCDI full battery from 0.3 to 5.0 A g⁻¹, The voltage range for the tests was 0 to 1.75 V. The impedance spectra were measured at Gamry with a frequency sweep range of 0.01 Hz to 100,000 Hz.

The electrochemical process of the (Na, Mn) V₈O₂₀·5H₂O electrode material involves eight electrons. We have recalculated the theoretical capacity based on this understanding, and it amounts to 239.3 mAh g⁻¹, F = Faraday constant (96485 C mol⁻¹), M = Molar mass (g mol⁻¹), n = Electron transfer number.

$$\text{Theoretical capacity (mAh g}^{-1}\text{)} = \frac{F \cdot n}{3.6 \cdot M} \quad (1)$$

Galvanostatic Intermittent Titration Technique (GITT): The thermodynamic voltage-composition relationship referring to the equilibrium phase diagram of the system was found using the GITT. The GITT data was used to compute the interfacial reaction resistances (R_s , cm^{-2}) of the Mn-NVO cathode during the charge/discharge operation. GITT tests were conducted under the current density (I) of 0.3 mA cm^{-2} to charge and discharge. First, the battery was discharging (charging) for 5 min, and then resting until the battery voltage stabilized (~ 10 min), continue discharging (charging) for 5 min, and repeat the above process until the cut-off voltage was $-0.7\text{--}1.2 \text{ V}$ (vs. Ag/AgCl). The reaction resistance can be calculated by the instantaneous voltage drop (ΔE) and current density (I) of discharge (charge)[26].

$$\Delta E = E_0 - E_1 = I * R_s \quad (2)$$

$$R_s = \frac{E_0 - E_1}{I} \quad (3)$$

3. Results and discussion

The transportation of Mg^{2+} ions through electrode materials can be challenging due to stronger electrostatic interactions. This can lead to issues such as strong polarization, electrolyte decomposition, irreversible phase transformations, or difficulties in intercalation within electrode materials during discharge-charge processes[27]. Therefore, we took advantage of the MSHBs, which use a $\text{Mg}^{2+}/\text{Na}^+$ hybrid electrolyte to enhance the kinetics of the Mg^{2+} ions, achieving excellent rate and cycling stability (Fig. 1)[28]. MSHBs are more advantageous in terms of economic and safety and are well suited for wide storage applications[29]. To

construct MSHBs, the rapid diffusion kinetics of Na ions were harnessed by incorporating them into MIBs through a dual salt electrolyte[30]. Besides, in a "rocking chair" type battery, both metal cations can be used as carriers and both ions take part in the half-cell reaction by the hybrid electrolyte[6]. The hybrid ion systems may improve rate performance due to the synergistic motion between ions that promote kinetics[6,31]. The MSHBs leverage the faster diffusion rate of Na⁺ in solids to improve the slow diffusion kinetics and enhance the rate performance in MIBs and maintain a relatively high specific capacity.

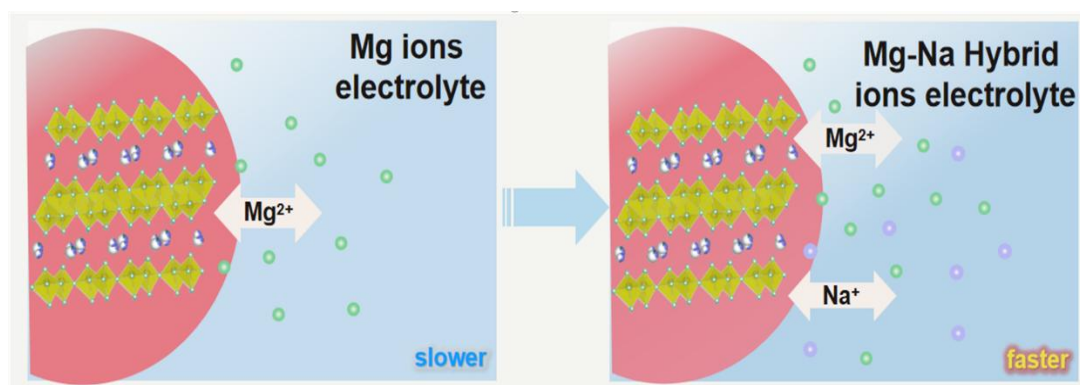


Fig. 1. Schematic diagram illustrates the inclusion of Na⁺ ions in MSHBs to facilitate enhance the inadequate rate performance of MIBs.

Layered vanadium oxide has demonstrated significant potential as a cathode material in magnesium ion batteries and was therefore chosen as the model material for this study[25,32]. The XRD pattern of the Mn-NVO was demonstrated in Fig. 2a, revealing a total of eight diffraction peaks observed at 2θ values of 8.2°, 24.7°, 25.6°, 33.1°, 34.6°, 41.8°, 50°, and 61.3°, corresponding to the reflection planes of (001), (003), (110), (004), (11 $\bar{3}$), (005), (020), and (024), consistent with the (Na, Ca)(V,

$\text{Fe}_8\text{O}_{20}\cdot n\text{H}_2\text{O}$ belonging to the $C2/m$ space group (JCPDS No. 45-1363)[33]. The well-defined and intense diffraction peaks indicate highly crystalline nature of Mn-NVO[23].

The morphology of Mn-NVO was explored using the scanning electron microscopy (SEM) and transmission electron microscope (TEM) measurements (Fig. 2a-b). As depicted in Fig. 2a, the Mn-NVO particles appear as uniform nanobelts. Fig. 2a presents the SEM image, revealing the Mn-NVO particles consist of nanobelts with a diameter of ranging from 150 to 250 nm, which agree with the TEM images (Fig. 2b). Besides, the high-resolution transmission electron microscopy (HRTEM) image captured in Fig. 2b, revealing the remarkably crystalline structure of Mn-NVO nanobelts. The crystal lattice in the image reveals interlayer distance of 0.21 nm and 0.15 nm, matching the (005) and (710) planes of NVO, respectively[22]. The TEM elemental mapping images (TEM-EDS) depicted in Fig. S1 reveal the homogeneous distributions of V, O, Na, and Mn within the Mn-NVO. Mn-NVO has a typical layered crystal structure, the introduction of Mn ion doping results in the displacement of Na (1) from its average position, and the position previously occupied by Na (1) is now taken over by Mn (1), demonstrating that Mn-NVO adopts the crystal structure of $(\text{Na}, \text{Mn})\text{V}_8\text{O}_{20}\cdot n\text{H}_2\text{O}$ (Fig. 2c)[34]. The nanoscale structure of Mn-NVO is considered to be useful in shortening the ion and electron transport paths and in helping attenuate the irreversible deformation caused by the polarization phenomenon[1]. In addition, since the doping amount of Mn is very limited, therefore its contribution to the capacity is negligible.

To determine the optimal amount of Na⁺ in the hybrid electrolyte, different concentrations of sodium salts (0.5 M, 1.0 M, and 1.5 M NaClO₄) were introduced into the Mg²⁺ based electrolyte (i.e., 1 M Mg (ClO₄)₂ in TEGDME : H₂O = 4 : 1), We selected TEGDME/H₂O (4:1) as the solvent ratio due to its ability to provide a larger electrochemical window and higher ionic conductivity [25, 35, 36]. Additionally, the electrochemical performance of the NVO cathode in different concentrations of Mg(ClO₄)₂ in the hybrid electrolyte was compared (Fig. S2). When utilizing 0.5 M, 1.0 M, and 1.5 M NaClO₄ in MSHBs, the discharge capacity of Mn-NVO exhibits a rise to 217.7 mAh g⁻¹, 238.5 mAh g⁻¹, and 243.6 mAh g⁻¹, respectively (Fig. S3). Mn-NVO presents great electrochemical activity when paired with a 1.5 M NaClO₄ electrolyte, so 1.5 M NaClO₄ in MSHBs was selected as the optimal electrolyte[10]. Besides, Fig. 2d the rate performance of the Mn-NVO cathode when tested with different electrolytes (i.e., 1 M Mg (ClO₄)₂, 1.5 M NaClO₄, and 1 M Mg (ClO₄)₂ + 1.5 M NaClO₄ in TEGDME : H₂O = 4 : 1). Rate performance of Mn-NVO cathode in MSHBs (1 M Mg (ClO₄)₂ + 1.5 M NaClO₄ in TEGDME : H₂O = 4 : 1) is better than that of the Mn-NVO in SIBs (1.5 M NaClO₄ in TEGDME : H₂O = 4 : 1) and MIBs (1 M Mg (ClO₄)₂ in TEGDME : H₂O = 4 : 1). At 300 mA g⁻¹, it exhibits a great capacity of 249.9 mAh g⁻¹. As discharge rates increase to 3000 mA g⁻¹, the capacity retains 130.2 mAh g⁻¹, implying the advantage of fast charging[37]. Besides, at 300 mA g⁻¹, it presents great capacity recoverability. By contrast, the Mn-NVO cathode in the SIBs exhibits a significantly lower capacity of 70.6 mAh g⁻¹ at 300 mA g⁻¹, which not be competitive for practical applications. Besides, the reversible capacities in the MIBs

can only maintain $\sim 71.8 \text{ mAh g}^{-1}$ at 3000 mA g^{-1} , which be attributed to inherently slow electrochemical kinetics. The impressive capacities for MIBs at less than 1000 mA g^{-1} provide evidence of the successful insertion of Mg^{2+} ions into the Mn-NVO cathode material. Nevertheless, as the current density further increases (*i.e.*, 1500 mA g^{-1} , 2000 mA g^{-1} , 2500 mA g^{-1} , 3000 mA g^{-1}), the specific capacity significantly decreases, showing a relatively low specific capacity. Rate performance of Mn-NVO cathode in MSHBs has excellent properties compared to MIBs, especially at high current densities[38]. This suggests that the Mg ions insert into the Mn-NVO cathode interlamination becomes challenging under significant polarization[8]. Additionally, the charge/discharge curves of the Mn-NVO cathode are 61.3 , 112.8 , and 145.2 mAh g^{-1} at 2000 mA g^{-1} in the SIBs, MIBs, and MSHBs, respectively (Fig. 2e). The MSHBs exhibit excellent specific capacity at higher currents, indicating their outstanding rate performance. Notably, MSHBs display a higher voltage plateau, suggesting a synergistic effect between magnesium and sodium ions[39]. In addition, MSHBs have two voltage platforms, which further demonstrates the co-intercalation of Mg^{2+} and Na^+ in the Mn-NVO cathode.

Fig. 2f displays the relevant charge/discharge profiles of the Mn-NVO cathode in MSHBs. The results show a discharge capacity of 249.9 mAh g^{-1} when operated at 300 mA g^{-1} . Notably, even under 3000 mA g^{-1} , it holds a discharge capacity of 130.2 mAh g^{-1} . Besides, the discharge capacities for MSIBs at 0.5 , 0.8 , 1 , 1.5 , 2 , and 2.5 A g^{-1} are 193 , 169.5 , 166 , 155 , 143.6 , and 136.8 mAh g^{-1} , respectively. The sloping charge-discharge plots observed indicate an ion (de)intercalation process

characterized by a solid-solution type behavior[40], which is better than those in MIBs and SIBs. This reveals that there is a synergistic effect between Mg^{2+} and Na^+ in the hybrid electrolyte. Simultaneously, after 1,500 cycles at 1.5 A g^{-1} , Mn-NVO cathode fluctuates slightly at the initial stage (~ 300 cycles) and fails quickly after 1500 cycles with a capacity decaying to 54.9 mAh g^{-1} in MIBs[41].

In addition, attenuation is only employed to reach capacity without impacting the well-shaped steady voltage plateau during the cycle process. (Fig. 2f)[41]. At higher current densities, it is likely that the NVO cathode may not undergo sufficient reaction, leading to discrepancies in the charge/discharge curves. This phenomenon can be attributed to several factors. Firstly, the rapid insertion of ions onto the surface of the NVO active material at higher current densities may result in the deactivation of the outermost layer. Consequently, subsequent ions may not have adequate time to migrate into the depths of the active material. Additionally, the heightened currents may induce a higher degree of disruption, increasing the likelihood of damaging the crystalline structure of the NVO cathode.

Although the Mn-NVO cathode presents good cycling stability in SIBs, its insufficient capacity (57.6 mAh g^{-1} after 1500 cycles) remains a challenge for widespread adoption in large-scale energy storage applications. While simple MIBs demonstrated high capacity, they faced challenges related to rate performance and cycle stability. Conversely, SIBs prepared with only sodium salt in the electrolyte showed poor capacity but exhibited excellent rate performance and cycle stability. To address these limitations, we adopted the strategy of MSHBs, combining the

advantages of both systems. The cell preserved 84.6 mAh g⁻¹ with near 100% coulombic efficiency, exhibiting both the structural stability of the Mn-NVO cathode and the cycling stability of the MSHBs (Fig. 2g)[42]. As a result, the stability of the Mn-NVO cathode in MSHBs can be attributed to a minimized presence of free water molecules, which minimizes irreversible parasitic reactions. And the emergence of synergistic effect between Mg²⁺ and Na⁺ ions.

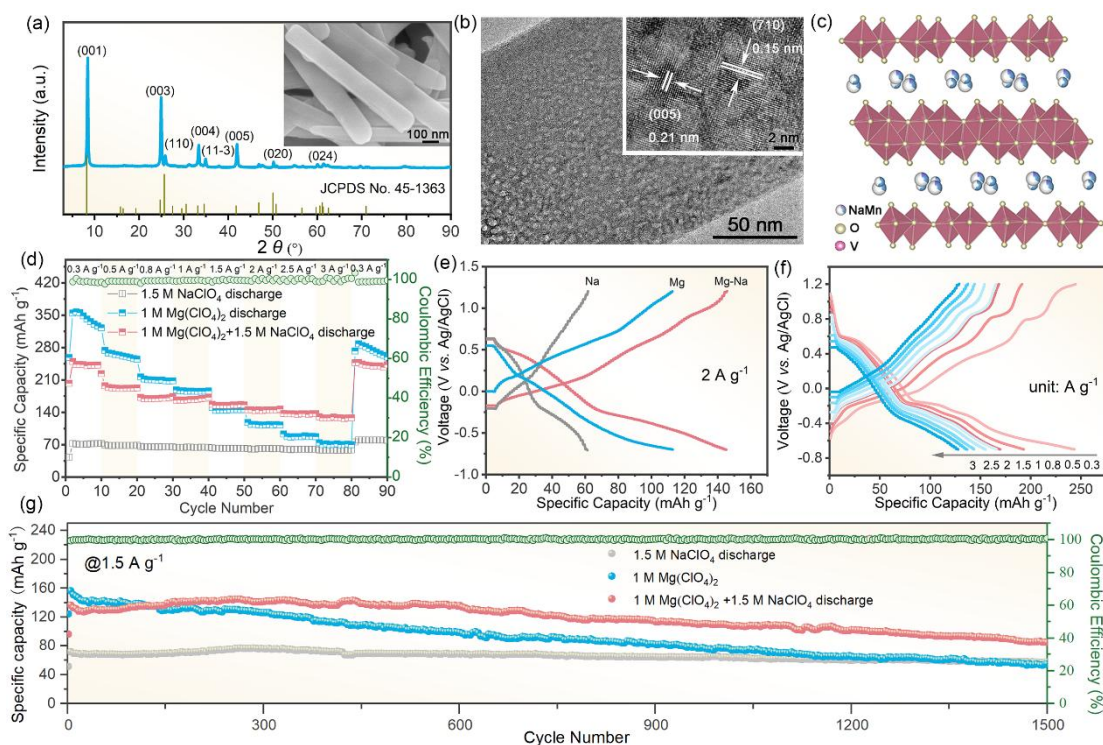


Fig. 2. (a) XRD diffraction pattern and SEM image of Mn-NVO; (b) TEM images and HRTEM images of Mn-NVO; (c) Crystal structure of Mn-NVO; (d) The rate performances of Mn-NVO cathode in SIBs, MIBs, and MSHBs, with the corresponding Coulombic efficiency in MSHBs shown on the right axis; (e) Discharge curves of the Mn-NVO cathode in SIBs, MIBs, and MSHBs; (f) Discharge-charge curves of the Mn-NVO cathode at various rates in MSHBs; (g) Cycling performance of Mn-NVO cathode in SIBs, MIBs, and MSHBs at 1.5 A g⁻¹.

In order to explore the kinetic variance, cyclic voltammetry (CV) curves were obtained for the Mn-NVO cathode in both MIBs and MSHBs are captured at 5.0 mV s⁻¹ (Fig. 3a)[25]. Indeed, the discharge specific capacity of MIBs is notably higher than that of MSHBs at low currents. However, the CV measurement reveals far more distinct redox peaks for Mn-NVO cathode in MSHBs related to the reversible reaction in comparison with that in MIBs, demonstrative of significantly superior kinetics and redox reversibility in MSHBs[38]. To disclose the causes of the great rate performance of MSHBs, the electrochemical kinetics were through CV curves from 1.0 to 5.0 mV s⁻¹ (Fig. 3b). Even at higher scan rates, the CV curves of the Mn-NVO cathode still retained clear redox peaks, implying a great rate capability[38]. Besides, just a small peak shift was observed within 1.0 to 5.0 mV s⁻¹, demonstrating a great electrochemical reversibility[43].

Generally, the correlation between peak currents (*i*) and the scan rates (*v*) can be mathematically represented by the following equation:

$$i = av^b[25] \quad (4)$$

Calculated *b* values in Fig. S4 are 0.67, 0.77, 0.70, and 0.82, respectively, implying a portion of the capacitive behavior reaction in MSHBs[44], which helps to the fast diffusion of ions to the Mn-NVO cathode[45]. Moreover, as demonstrated in Fig. 3c, minimal shifts in peak potentials (< 0.15 V) are discovered for both cathodic and anodic peaks from 1.0 to 5.0 mV s⁻¹, which benefits fast energy storage[43]. The initial five CV curves achieved at 1 mV s⁻¹ with different sodium content hybrid

electrolytes of the Mn-NVO cathode are revealed in Fig. S5 and Fig. S6. The CV curve of the second cycle for the Mn-NVO cathode closely resembles that of the first cycle, indicating good cycling stability. During the initial cathodic scan, the Mn-NVO cathode displayed four distinct cathode peaks at potential values of 0.94 V, 0.70 V, 0.61 V, and 0.37 V. Subsequent anodic scans exhibited four peaks at 0.49 V, 0.71 V, 0.92 V, and 1.1 V. These profiles suggest multiple phase transitions, a characteristic feature of Na⁺ intercalation in layered materials. The presence of both reduction and oxidation peaks in pairs signifies a multi-step reaction mechanism associated with the co-insertion/extraction of Mg²⁺/Na⁺ ions, which is unlike the V₂O₅ based electrodes that present two representative pairs of redox peaks[46].

The galvanostatic intermittent titration technique (GITT) was employed to conduct in situ monitoring of the interfacial reaction resistances during diverse (dis)charge stages of the Mn-NVO electrode. For the GITT measurements, a pulse duration of 5 minutes with a rest period of 10 minutes was used to collect the potential response while applying a current density of 0.3 mA cm⁻²(Fig. 3d). Fig. 3e shows reaction resistances derived from the (dis)charge operations. It appears that the reaction resistances experience a slight decrease during the first discharge potential (0.7 – -0.2 V vs Ag/AgCl), followed by significant raise during the final discharge potential (-0.2 – -0.7 V vs Ag/AgCl). Furthermore, this process exhibits reversibility during the charging process, confirming that the changes occurring in the Mn-NVO electrode are periodic and reversible[26].

Briefly, the addition of Na^+ enhances the structural stability, promoting the dynamics of the Mg^{2+} reaction, and improving the reversibility[47]. Moreover, the higher non-diffusion limited capacity contributions as well as outstanding dynamic behavior allow excellent electrochemistry performance of the Mn-NVO cathode in MSHBs[43].

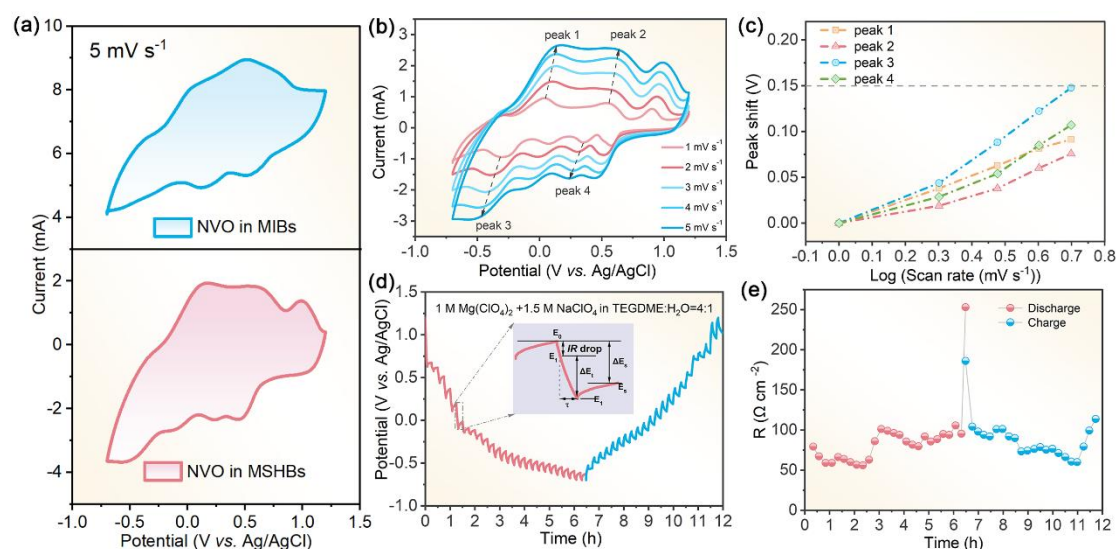


Fig. 3. (a) Contrast of two CV curves of the half-cells in MIBs and MSHBs at 5.0 mV s^{-1} ; (b) CV of Mn-NVO at $1.0, 2.0, 3.0, 4.0,$ and 5.0 mV s^{-1} in MSHBs; (c) Cathodic peak potential shifts vs log (scan rate) curves; (d) GITT curves and (e) Changes in reaction resistance during the discharge/charge process of a half-cell in MSHBs at 0.3 mA cm^{-2} .

To better perceive the ion storage mechanism of Mn-NVO cathode in MSHBs, the investigation of the reaction mechanisms involved *ex-situ* XRD and the related charge-discharge curve at 0.2 A g^{-1} and *ex-situ* XPS (Fig. 4)[48]. The *ex-situ* XRD patterns of MIBs and MSHBs are indicated in Fig. 4a-d [49]. Firstly, *ex-situ* XRD

patterns of Mn-NVO in MIBs at the states as marked in Fig. 4a are exhibited in Fig. 4b[30]. As observed in Fig. 4a and Fig. 4b, the XRD is relatively reversible in the initial cycle in MIBs as discussed in the previous work[25]. The irreversibility of XRD in the second cycle suggests that there is a need to improve the reversibility and stability of Mn-NVO in MIBs. The unfriendly reversibility and structural change during the second cycle process may be caused by two points: One reason is that the inserting Mg^{2+} into the Mn-NVO cathode leads to larger phase and crystal structure changes, which destroys the original structure; Additionally, the insertion of Mg^{2+} can cause lattice strain in the Mn-NVO cathode, leading to distortion within its lattice structure. Both of these causes can lead to a structural collapse or a pulverization of the Mn-NVO cathode in MIBs, resulting in the poor reversibility and cycling stability[50].

Next, we adopted the strategy of MSHBs to solve the problems associated with MIBs. Fig. 4c and Fig. 4d present the charge-discharge curves of Mn-NVO and related sites that were investigated using *ex-situ* XRD analysis to explore its structural change in MSHBs[30]. Firstly, the pristine material well matches the $(Na, Ca)(V, Fe)_8O_{20} \cdot nH_2O$ with the $C2/m$ space group (JCPDS No. 45-1363)[33], which is consistent with Mn-NVO (Fig. 4d)[34]. The initial Mn-NVO is filled with Na^+ . The purpose of first charging is to allow extraction of the Na^+ ions from the interlayer, which provide space for the following intercalation of Mg^{2+} and Na^+ . When compared to the initial Mn-NVO cathode, a new phase appears at 5.3° , 10.7° and 21.1° for the first full charged $(C_{2.7}H_{8.1}O_{1.35}S_{1.35}!V_2O_5)$, JCPDS No. 45-1529), it returned to its

original position of 8.1° after discharge after the subsequent fully discharged and remains reversible in the second cycles. Therefore, throughout the charging and discharging processes, a reversible phase transition process existed, demonstrating an outstanding structural stability and reversibility of the Mn-NVO cathode with respect to the host material in MSHBs[42].

Moreover, *ex-situ* XRD measurement were conducted at various discharge/charge states to investigate the storage mechanism of MSHBs and SIBs (Fig. S7). The *ex-situ* XRD in the SIBs exhibits good reversibility (Fig. S8). Fig. S9 displays the *ex-situ* XRD of cathode in pure aqueous electrolyte (1 M Mg $(\text{ClO}_4)_2 \cdot 6\text{H}_2\text{O}$ + 1.5 M NaClO₄ in H₂O), and it is obvious that the structural changes are irreversible during the process of charging and discharging, most likely owing to water damaging the cathode structure. It proves that the added organic solvent TEGDME is also important for stability during cycling. This finding implies that the addition of sodium salts to the MIBs and the retention of Na⁺ and Mg²⁺ in the interlayer space of Mn-NVO may be critical to the cycling performance, which significantly enhances the capacity retention although a portion of the capacity at low current densities is sacrificed[6]. A portion of Na⁺ and Mg²⁺ as the pillar can keep the Mn-NVO cathode crystal structural stability throughout the cycling process, which can also lead to reduced strain during the Na⁺ and Mg²⁺ insertion/extraction, so the stability and reversibility are improved[47]. Besides, we consider the storage mechanism for both Na⁺ and Mg²⁺ is an intercalation reaction, may consistent with the "rocking chair" theory.

Ex-situ XPS investigations were conducted to investigate the ion storage mechanism of the Mn-NVO cathode in MSHBs. On the initial few cycles, Ar⁺ ion sputtering was also carried out (Fig. 4e)[25]. There is no Mg 1s signal in the initial Mn-NVO cathode. At fully discharged, the peak intensity arrives its highest point (discharge to -0.7 V). This observation suggests that Mg²⁺ has been inserted into the Mn-NVO cathode during the discharge process. Moreover, in the fully charged state (charge to 1.2 V), the Mg²⁺ content decreases to a lower value. However, a few of Mg²⁺ that stays within the crystal lattice of the fully charged Mn-NVO cathode acts as pillar ions alongside Na⁺ to augment the rate capability and cycling stability of the Mn-NVO cathode. The result indicates a reversible process of Mg²⁺/Na⁺ insertion and extraction of the Mn-NVO cathode in MSHBs[47].

Besides, the XPS spectra obtained from the Mn-NVO cathodes at various charge and discharge states can also further verify the type of intercalated ions. As demonstrated in Fig. 4e, when the Mn-NVO cathode is discharged to -0.7 V, there is a noticeable intensification of the peaks corresponding to Na 1s and Mg 2p in the XPS spectra, implying co-insertion of Mg²⁺/Na⁺ into the Mn-NVO during the discharge process. Conversely, when the Mn-NVO cathode is charged to 1.2 V, the distinctive peaks associated with Na 1s and Mg 2p are attenuated, revealing Mg²⁺ and Na⁺ have been extracted from the Mn-NVO (Table S2). Moreover, in the fully charged state, there is still a minor presence of Mg²⁺ and Na⁺ within the crystal lattice of the Mn-NVO cathode. This occurrence can be associated to the electrostatic interaction between Mg²⁺/Na⁺ and lattice oxygen[10]. By analyzing *ex-situ* XPS, it is evident that

Na and Mg elements still exist in some unrecovered residual chemical states. Because of the consistent and regular change seen in numerous elements during the charging and discharging processes in MSHBs, it is still possible to draw the general conclusion of high reaction reversibility[47].

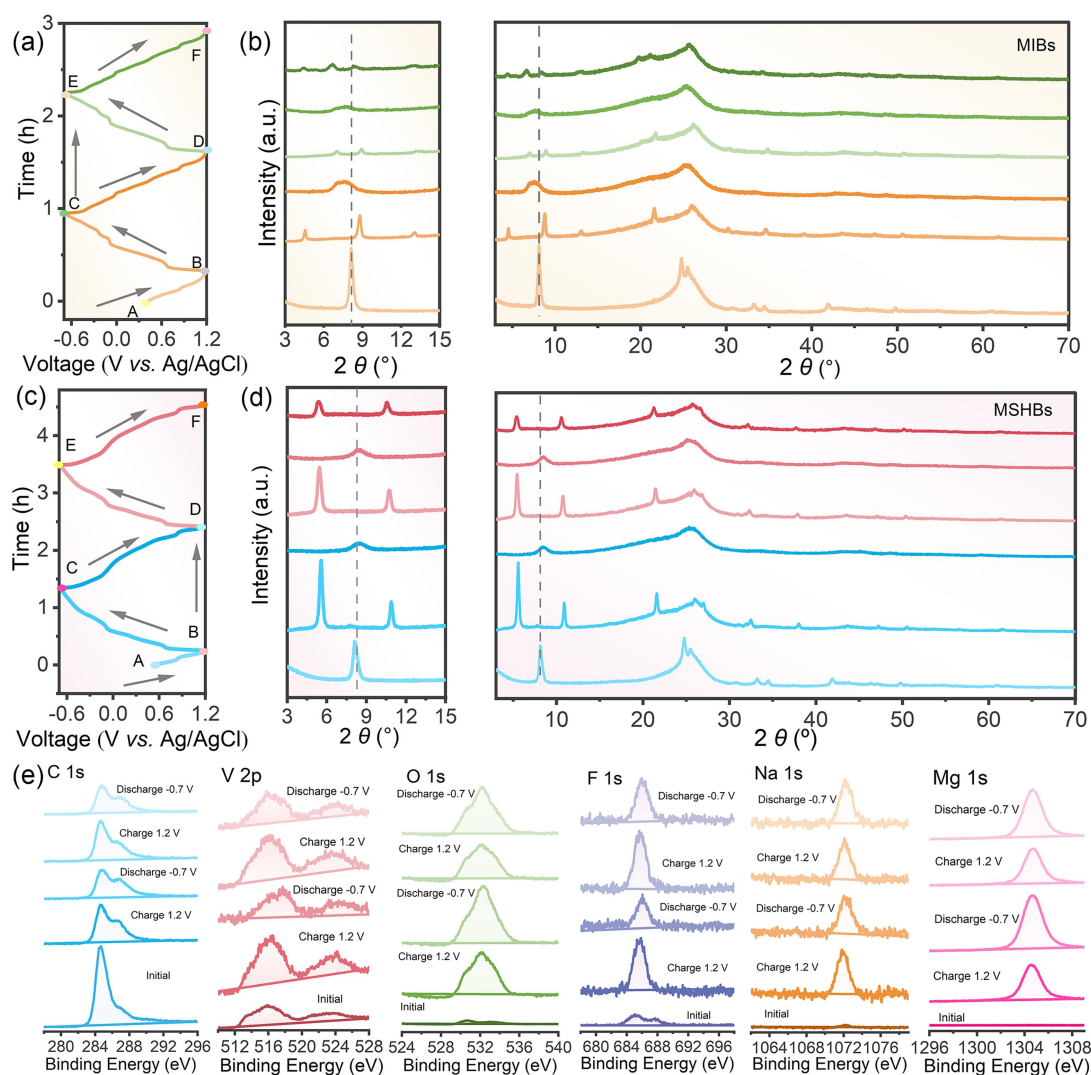


Fig. 4. (a) The initial two voltage-time curves of Mn-NVO cathode in MIBs (0.2 A g^{-1}); (b) corresponding ex-situ XRD patterns of the Mn-NVO cathode taken at the indicated points in (a); (c) The initial two voltage-time profiles of Mn-NVO cathode in MSHBs (0.2 A g^{-1}); (d) Corresponding ex-situ XRD patterns of the Mn-NVO cathode taken at the indicated points in (c); (e) XPS depth profiling of C 1s, V 2p, O

1s, F 1s, Na 1s, and Mg 1s after 140 s for the initial, the first fully charged, the first fully discharged, the second fully charged, the second fully discharged states, and the third fully charged.

Fig. 5 presents the findings from HRTEM characterizations and TEM-EDS element mapping, focusing on the distributions of the elements V, O, Na, and Mg. These techniques were employed to investigate the reaction mechanisms of the Mn-NVO cathode within the MSHBs[19]. As displayed in Fig. 5a-g, the HRTEM of initial Mn-NVO presents great crystallinity of the Mn-NVO cathode. The interplanar spacing of the crystal was found to be 1.08 nm, which corresponds to the (0 0 1) plane of Mn-NVO[10]. Upon reaching the first fully charged state, the interplanar spacing of the crystal changed to 0.83 nm as a result of the deintercalation of Na⁺ ions, corresponding to the (002) plane for solvent intercalation of V₂O₅. Subsequently, the interplanar distance of the crystal returned to the initial 1.08 nm with the intercalation of Na⁺ and Mg²⁺ at the first discharged, and maintained a reversible transition during the subsequent cycle process, which confirmed the *ex situ* XRD result[25]. The SEM images of different states (initial, first charge, first discharge, second charge, second discharge, and third charge states) in Mn-NVO cathodes and MSHBs are shown in Fig. S10. Even and continuous cathode electrolyte interface (CEI) film is present on the cathode surface during cycling, and the addition of TEGDME organic solvent contributes to the stability of the cathode material during cycling[25].

TEM-EDS mapping enables the identification of Mg and Na elements within the

Mn-NVO cathode when in a discharged state. This presents obvious visual evidence that $\text{Mg}^{2+}/\text{Na}^+$ was inserted into the lattice structure of the cathode material (Fig. 5b-h)[51]. The intensity of the Mg element decreases and increases regularly during charge and discharge in MSHBs, demonstrating the deintercalation and intercalation of Mg^{2+} in the Mn-NVO cathode, respectively[51]. Besides, the intensity of Na decreases and increases weakly during the charge and discharge, which implies that there is a co-deintercalation/intercalation of Mg^{2+} and Na^+ in the Mn-NVO cathode. Specifically, as displayed by the TEM-EDS results in MSHBs (Fig. 5i and Table S3), the Mg content from the initial to the second charged state is 0, 1.55, 2.60, and 1.04 at%. Furthermore, the Na contents from the initial to the second charged state are 5.62, 0.84, 1.30, and 1.27 at%. This is obviously not the same as how MIBs charge and discharge. Besides, the residual Mg^{2+} and Na^+ were discovered in a charged state. These ions act as columnar ions, playing a vital role in stabilizing the structure of the cathode material. This enhanced structural stability, resulting in great cycling and rate performance[25].

Figure 5j illustrates the reaction mechanism of MSHBs and demonstrates the simultaneous co-intercalation of Na^+ and Mg^{2+} ions within the Mn-NVO cathode[33]. The presence of Na^+ and Mg^{2+} in the Mn-NVO cathode acts as the structure stabilizing “pillars”. These ions maintain the structural stability of the cathode during cycling by reducing the polarization interaction between ions and the cathode. Moreover, this contributes to enhanced cycling stability and rate performance in MSHBs[47].

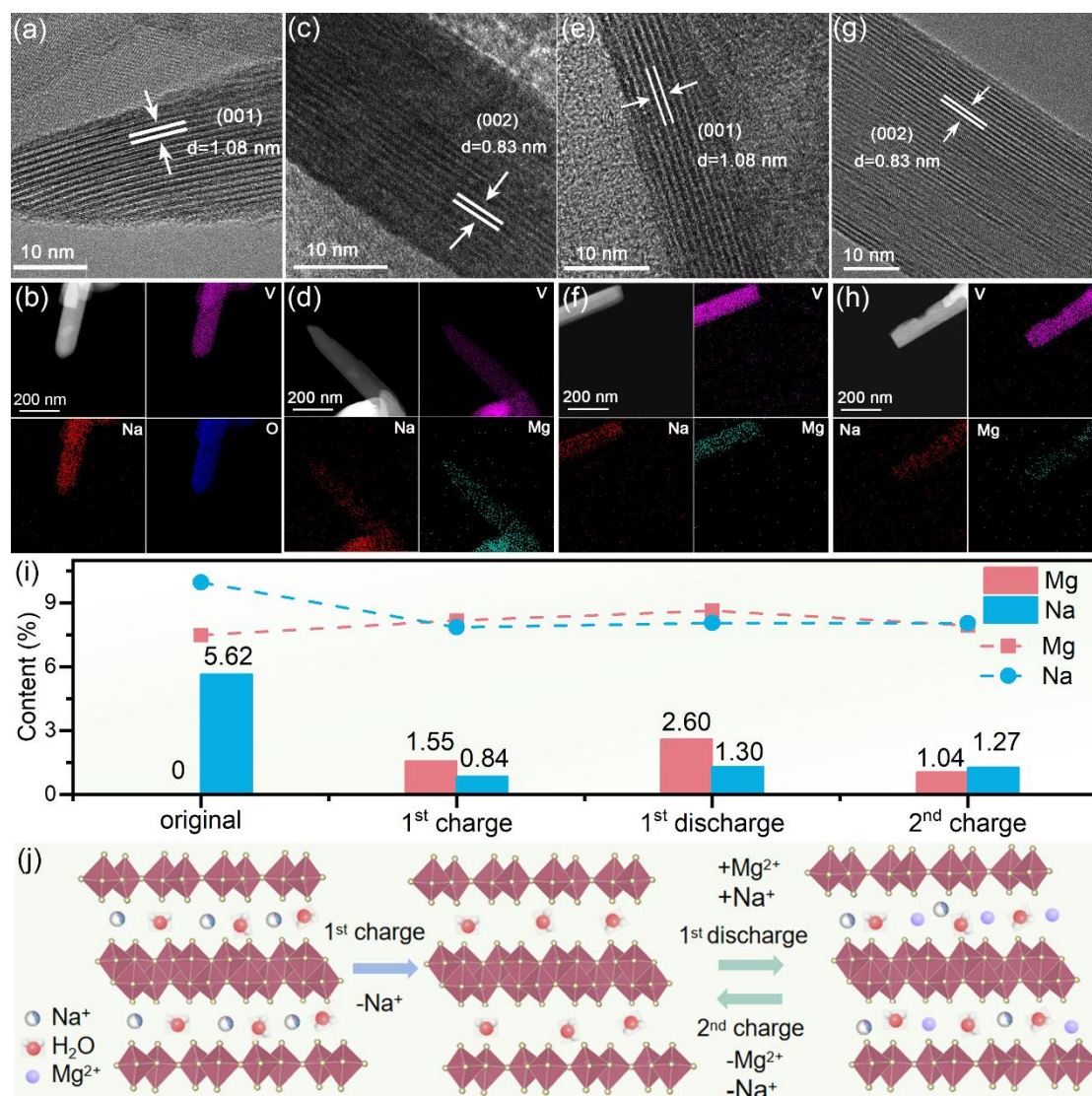


Fig. 5. (a-h) HRTEM images of Mn-NVO cathode and corresponding TEM-EDS element mapping are provided for different states (initial, 1st charged, 1st discharged, and 2nd charged state) in MSHBs, respectively; (i) TEM-EDS element comparison on Mn-NVO cathode in different states: initial, 1st charged, 1st discharged, and 2nd charged state. (j) A schematic diagram illustrates the mechanism of the Na⁺ extraction from the Mn-NVO cathode, as well as the subsequent Mg²⁺/Na⁺ co-insertion charge/discharge process.

The electrochemical performance of Mn-NVO cathodes was explored using CR2032 coin cells, where organic PTCDI served as the anode material and 1 M Mg (ClO₄)₂+1.5 M NaClO₄ in TEGDME: H₂O = 4 : 1 as electrolytes. To address the challenges posed by slow kinetics and inadequate rate performance in MIBs, leveraging low-cost and abundantly available MSHBs is imperative. The selection of commercial organic PTCDI as the anode material for MSHBs was based on its favorable characteristics, including a low reaction potential (-0.6 V vs. SHE) and theoretical capacity of 137 mAh g⁻¹, considering a two-electron transfer per carbonyl group.[52]

Besides, the PTCDI anode also exhibits great cycling stability when utilized as a Mg/Na ion storage anode[42]. The working principle of the MSHBs is shown in Fig. 6a, which reflects that the MSHBs can achieve Mg²⁺/ Na⁺ co-(de)intercalating into the host materials during the charging and discharging process[8]. XRD pattern of PTCDI anode is demonstrated in Fig. S11. To evaluate the feasibility of PTCDI in MSHBs, the relevant tests in Fig. 6b-c demonstrate that it exhibits excellent electrochemical activity in MSHBs[52]. The CV curves of the organic PTCDI anode in MSHBs exhibit a slight peak shift and an increase in peak intensity with increased scan rates, which demonstrates the fast kinetics of organic PTCDI anode in MSHBs (Fig. 6b)[12]. The CV curves of the organic PTCDI anode in SIBs and MIBs are also exhibited in Fig. S12 and Fig. S13. Besides, Fig. 6c presents the rate performance of the PTCDI anode in the MSHBs. The PTCDI anode in the MSHBs displayed reversible capacities of 101.7 mAh g⁻¹ at 0.3 A g⁻¹ and 61.1 mAh g⁻¹ at 3.0 A g⁻¹, showing the

reversibility and fast kinetics of ion storage[25]. The CV curves of Mn-NVO//PTCDI full battery kept their shapes from 1.0 to 5.0 mV s^{-1} (Fig. 6d)[42]. Additionally, the CV and charge–discharge curves of Mn-NVO, PTCDI, and the full battery indicate that the assembled full battery can operate within a broad working voltage window spanning from 0 and 1.8V (Fig. S14)[53]. Fig. 6e further reveals the rate performance of the Mn-NVO//PTCDI full cells utilizing Mg/Na hybrid electrolytes at 0.1 A g^{-1} and 2 A g^{-1} . The reversible capacities achieved at these rates were 97.7 mAh g^{-1} and 57.2 mAh g^{-1} , respectively[54, 55]. The enhanced capacity can be related to the activation of the electrode material during the first 10 cycles[1, 56]. In addition, the EIS of the Mn-NVO//PTCDI full cell as shown in Fig. S15 can indicate the accelerated kinetics of the MSHBs compared to the MIBs.

The Mn-NVO//PTCDI full cells indicate outstanding electrochemical performance, surpassing the results reported in previous research on MSHBs (*i.e.* $\text{FeS}_2//\text{Mg}$ [21], $\text{Na}_2\text{VTi}(\text{PO}_4)_3//\text{Mg}$ [22], $\text{Mn}_3\text{O}_4//\text{NaTi}_2(\text{PO}_4)_3$ [23], $\text{Mg}_{1.5}\text{VCr}(\text{PO}_4)_3//\text{FeVO}_4$ [20] and $\text{FeFe}(\text{CN})_6//\text{Mg}$ [24]) (Fig. 6f and Table S1)[18]. In addition, NVO//PTCDI full cell also preserved the discharge capacity of 77.4 mAh g^{-1} after 10,000 cycles at 1 A g^{-1} , confirming great cycling stability of the full cell (Fig. 6g)[4]. In the first few cycles, the low coulomb efficiency and discharge capacity can be ascribed to the difficulty of ion intercalation. When the electrode material is activated, the occurrence of side reactions between the electrode material and the electrolyte diminishes, resulting to an enhancement in the chemical reaction as the active sites become more exposed[1]. Fig. S16 illustrates the charge-discharge

voltage curves of Mn-NVO//PTCDI full MSHBs at several cycle numbers, demonstrating excellent cycle stability. Furthermore, we conducted a comparative analysis of the energy density of the full battery with recent reported works, as shown in Fig. S17 and Table S4. Remarkably, the cells in this study exhibit a higher energy density (97.7 Wh kg^{-1}) in comparison to the other magnesium-based cells. This outcome underscores the exceptional electrochemical performance of MSHBs, revealing a promising design approach for rechargeable batteries in practical energy storage applications[57, 58].

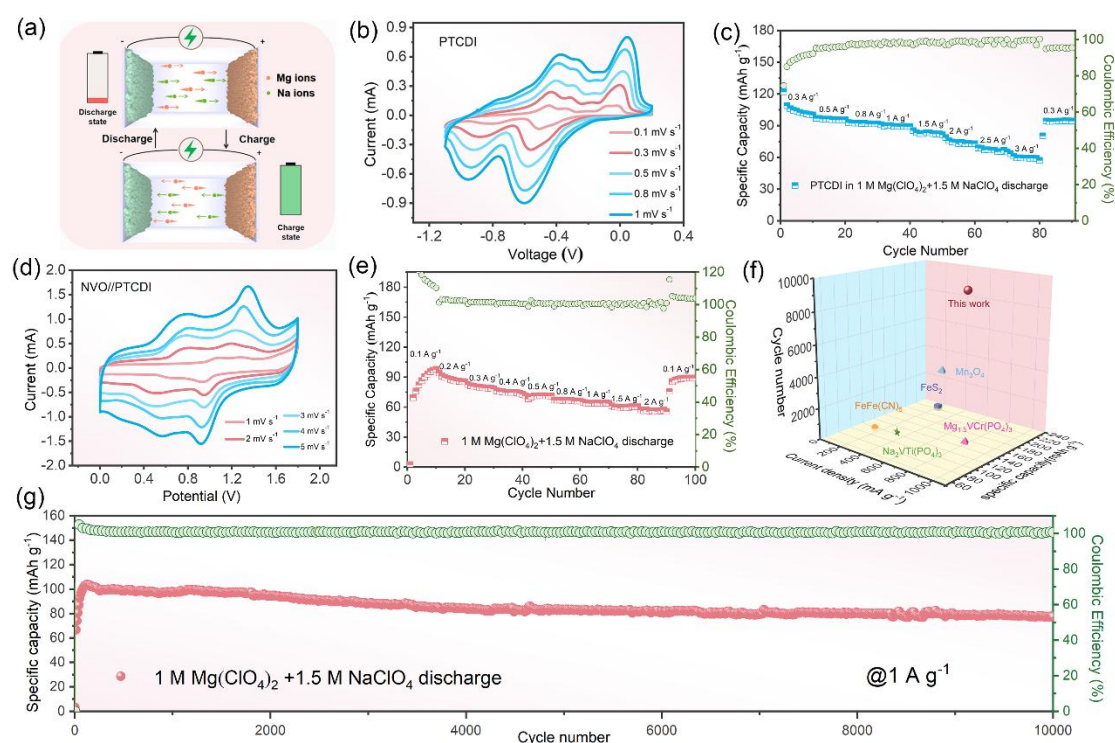


Fig. 6. Comprehensive performance of the full MSHBs: (a) Schematic depiction for the charge and discharge processes of the MSHBs; (b) CV of PTCDI anode (within -1.1-0.2 V) at 0.1, 0.3, 0.5, 0.8 and 1.0 mV s⁻¹ in MSHBs; (c) Rate performance of PTCDI anode from 0.3 A g⁻¹ to 3.0 A g⁻¹; (d) CV of Mn-NVO//PTCDI full battery

within 0-1.75 V in MSHBs at 1.0, 2.0, 3.0, 4.0 and 5.0 mV s⁻¹; (e) Rate performance of Mn-NVO//PTCDI from 0.1 A g⁻¹ to 2.0 A g⁻¹; (f) Electrochemical performance comparison of Mn-NVO//PTCDI with others for MSHBs reported in literature; (g) The cycling performance of the Mn-NVO//PTCDI full battery at 1 A g⁻¹.

4. Conclusions

Briefly, a novel MSHB has been developed, incorporating Mn-NVO as the cathode and PTCDI as the anode, paired with a hybrid electrolyte consisting of 1.5 M NaClO₄ + 1.0 M Mg (ClO₄)₂ in TEGDME: H₂O = 4 : 1. The environmental friendliness and earth-rich composition are clear advantages of MSHBs. Significantly, a synergistic effect emerges between the Mn-NVO cathode and hybrid electrolyte, playing a crucial role in enabling rapid and stable storage of Mg²⁺ and Na⁺ ions. Simultaneously, the Mn-NVO cathode presents a great discharge-specific capacity (249.9 mAh g⁻¹ at 0.3 A g⁻¹), high-rate capability (130.2 mAh g⁻¹ at 3 A g⁻¹), and remarkable cycling stability in MSHBs (1,500 cycles at 1.5 A g⁻¹). Furthermore, the Mn-NVO//PTCDI full battery has an exceptional cyclic stability of 10,000 cycles at 1.0 A g⁻¹. Overall, we expect that this work will demonstrate the potential of MSHBs with excellent electrochemical properties and cost-effective characteristics to enhance the cycling stability and rate capability of conventional MIBs and boost the progress of aqueous hybrid batteries.

CRedit authorship contribution statement

X. Wang: Validation, Formal Analysis, Investigation, Data curation, Writing-Original Draft. **T. Li:** Validation, Investigation. **X. Zhang:** Investigation, Validation. **Y. Wang:** Investigation, Validation. **H. Li:** Investigation, Methodology. **H.-F. Li:** Writing e review & editing. **G. Zhao:** Methodology, Validation, Writing e review & editing. **C. Han:** Conceptualization, Methodology, Validation, Writing e review & editing, Project administration, Supervision.

Declaration of competing interest

The authors declare that they have no known competing financial interests or personal relationships that could have appeared to influence the work reported in this paper.

Acknowledgments

We acknowledge the financial support from the National Natural Science Foundation of China (22109134, 22005207, 52261160384), and Guangdong Basic and Applied Basic Research Foundation (2019A1515011819), the Outstanding Youth Basic Research Project of Shenzhen (RCYX20221008092934093), Joint Funds of the National Natural Science Foundation of China (No. U22A20140), and the Science and Technology Development Fund, Macao SAR (File Nos. 0090/2021/A2 and 0049/2021/AGJ).

Appendix A. Supplementary data

Supplementary data to this article can be found online at xxx

References

- [1] X. Cheng, Z. Zhang, Q. Kong, Q. Zhang, T. Wang, S. Dong, L. Gu, X. Wang, J. Ma, P. Han, H.-j. Lin, C.-T. Chen, G. Cui, *Angew. Chem. Int. Ed. Engl.* 59 (2020) 11477-11482.
- [2] G. Liu, Y. Tang, H. Li, J. He, M. Ye, Y. Zhang, Z. Wen, X. Liu, C. C. Li, *Angew. Chem. Int. Ed. Engl.* 62 (2023) e202217945.
- [3] S. Ding, X. Dai, Z. Li, C. Wang, A. Meng, L. Wang, G. Li, J. Huang, S. Li, *Energy Storage Mater.* 47 (2022) 211-222.
- [4] Y. Xu, W. Cao, Y. Yin, J. Sheng, Q. An, Q. Wei, W. Yang, L. Mai, *Nano Energy* 55 (2019) 526-533.
- [5] W. Chen, X. Zhan, R. Yuan, S. Pidaparthy, A. X. B. Yong, H. An, Z. Tang, K. Yin, A. Patra, H. Jeong, C. Zhang, K. Ta, Z. W. Riedel, R. M. Stephens, D. P. Shoemaker, H. Yang, A. A. Gewirth, P. V. Braun, E. Ertekin, J.-M. Zuo, Q. Chen, *Nat. Mater.* 22 (2023) 92-99.
- [6] Z. Yang, X.-H. Liu, X.-X. He, W.-H. Lai, L. Li, Y. Qiao, S.-L. Chou, M. Wu, *Adv. Funct. Mater.* 31 (2021) 2006457.
- [7] Y. Zhang, Z. Yuan, L. Zhao, Y. Li, X. Qin, J. Li, W. Han, L. Wang, *Small* (2023) 2301815.
- [8] X. Yu, G. Zhao, C. Liu, C. Wu, H. Huang, J. He, N. Zhang, *Adv. Funct. Mater.* 31 (2021) 2103214.
- [9] C. Pérez-Vicente, S. Rubio, R. Ruiz, W. Zuo, Z. Liang, Y. Yang, G. F. Ortiz, *Small* 19 (2023) 2206010.
- [10] D. Wu, F. Wang, H. Yang, Y. Xu, Y. Zhuang, J. Zeng, Y. Yang, J. Zhao, *Energy Storage Mater.* 52 (2022) 94-103.
- [11] S. Rubio, R. Liu, X. Liu, P. Lavela, J. L. Tirado, Q. Li, Z. Liang, G. F. Ortiz, Y. Yang, *J. Mater. Chem. A* 7 (2019) 18081-18091.

- [12]Z. Chen, Q. Yang, D. Wang, A. Chen, X. Li, Z. Huang, G. Liang, Y. Wang, C. Zhi, *ACS Nano* 16 (2022) 5349-5357.
- [13]C.-H. Shin, H.-Y. Lee, C. Gyan-Barimah, J.-H. Yu, J.-S. Yu, *Chem. Soc. Rev.* 52 (2023) 2145-2192.
- [14]Y. Xu, Z. Liu, X. Zheng, K. Li, M. Wang, W. Yu, H. Hu, W. Chen, *Adv. Energy Mater.* 12 (2022) 2103352.
- [15]Y. Liu, W. Zhao, Z. Pan, Z. Fan, M. Zhang, X. Zhao, J. Chen, X. Yang, *Angew. Chem. Int. Ed. Engl.* 62 (2023) e202302617.
- [16]S. Zhang, Y. Wang, Y. Sun, Y. Wang, Y. Yang, P. Zhang, X. Lv, J. Wang, H. Zhu, *Y. NuLi, Small* 19 (2023) 2300148.
- [17]Y. Han, G. Li, Z. Hu, F. Wang, J. Chu, L. Huang, T. Shi, H. Zhan, Z. Song, *Energy Storage Mater.* 46 (2022) 300-312.
- [18]H. Xu, X. Zhang, T. Xie, Z. Li, F. Sun, N. Zhang, H. Chen, Y. Zhu, X. Zou, C. Lu, J. Zou, R. M. Laine, *Energy Storage Mater.* 46 (2022) 583-593.
- [19]Y. Ding, T. Han, Z. Wu, Y. Guan, J. Hu, C. Hu, Y. Tian, J. Liu, *ACS Nano* 16 (2022) 15369-15381.
- [20]Y. Tang, X. Li, H. Lv, W. Wang, Q. Yang, C. Zhi, H. Li, *Angew. Chem. Int. Ed. Engl.* 60 (2021) 5443-5452.
- [21]M. Walter, K. V. Kravchyk, M. Ibáñez, M. V. Kovalenko, *Chem. Mater.* 27 (2015) 7452-7458.
- [22]Y. Zhang, J. Gui, T. Li, Z. Chen, S.-a. Cao, F. Xu, *Chem. Eng. J.* 399 (2020) 125689.
- [23]X. Cao, L. Wang, J. Chen, J. Zheng, *J. Mater. Chem. A* 6 (2018) 15762-15770.
- [24]H. Dong, Y. Li, Y. Liang, G. Li, C.-J. Sun, Y. Ren, Y. Lu, Y. Yao, *Chem. Commun.* 56 (2016) 8263-8266.
- [25]X. Wang, X. Zhang, G. Zhao, H. Hong, Z. Tang, X. Xu, H. Li, C. Zhi, C. Han, *ACS Nano* 16 (2022) 6093-6102.
- [26]S. Li, J. Shang, M. Li, M. Xu, F. Zeng, H. Yin, Y. Tang, C. Han, H.-M. Cheng, *Adv. Mater.* (2022) 2207115.

- [27] S. Hou, X. Ji, K. Gaskell, P.-f. Wang, L. Wang, J. Xu, R. Sun, O. Borodin, C. Wang, *Science* 374 (2021) 172-178.
- [28] P. Wang, J. Trück, J. Häcker, A. Schlosser, K. Küster, U. Starke, L. Reinders, M. R. Buchmeiser, *Energy Storage Mater.* 49 (2022) 509-517.
- [29] M. Karlsmo, R. Bouchal, P. Johansson, *Angew. Chem. Int. Ed. Engl.* 60 (2021) 24709-24715.
- [30] G. Zhu, G. Xia, H. Pan, X. Yu, *Adv. Sci.* 9 (2022) 2106107.
- [31] X. Zhao, J. Yan, H. Hong, Y. Zhao, Q. Li, Y. Tang, J. He, Z. Wei, S. He, X. Hou, C. Zhi, H. Li, *Adv. Energy Mater.* 12 (2022) 2202478.
- [32] X. Xu, F. Xiong, J. Meng, X. Wang, C. Niu, Q. An, L. Mai, *Adv. Funct. Mater.* 30 (2020) 1904398.
- [33] C. Wang, L. Zhang, M. Al-Mamun, Y. Dou, P. Liu, D. Su, G. Wang, S. Zhang, D. Wang, H. Zhao, *Adv. Energy Mater.* 9 (2019) 1900909.
- [34] M. Du, C. Liu, F. Zhang, W. Dong, X. Zhang, Y. Sang, J.-J. Wang, Y.-G. Guo, H. Liu, S. Wang, *Adv. Energy Mater.* 7 (2020) 2000083.
- [35] Y. Dong, L. Miao, G. Ma, S. Di, Y. Wang, L. Wang, J. Xu, N. Zhang, *Chem. Sci.*, 12 (2021) 5843-5852.
- [36] G. Ma, L. Miao, Y. Dong, W. Yuan, X. Nie, S. Di, Y. Wang, L. Wang, N. Zhang, *Energy Storage Mater.* 47 (2022) 203-210.
- [37] C. Yang, Z. Pu, Z. Jiang, X. Gao, K. Wang, S. Wang, Y. Chai, Q. Li, X. Wu, Y. Xiao, D. Xu, *Adv. Energy Mater.* 12 (2022) 2201718.
- [38] Y. Cao, Y. Zhu, C. Du, X. Yang, T. Xia, X. Ma, C. Cao, *ACS Nano* 16 (2022) 1578-1588.
- [39] Y. Yang, G. Qu, H. Wei, Z. Wei, C. Liu, Y. Lin, X. Li, C. Han, C. Zhi, H. Li, *Adv. Energy Mater.* 13 (2023) 2203729.
- [40] Y. Zhu, J. Yin, X. Zheng, A.-H. Emwas, Y. Lei, O. F. Mohammed, Y. Cui, H. N. Alshareef, *Energy Environ. Sci.* 14 (2021) 4463-4473.
- [41] X. Li, Q. Li, Y. Hou, Q. Yang, Z. Chen, Z. Huang, G. Liang, Y. Zhao, L. Ma, M. Li, Q. Huang, C. Zhi, *ACS Nano* 15 (2021) 14631-14642.

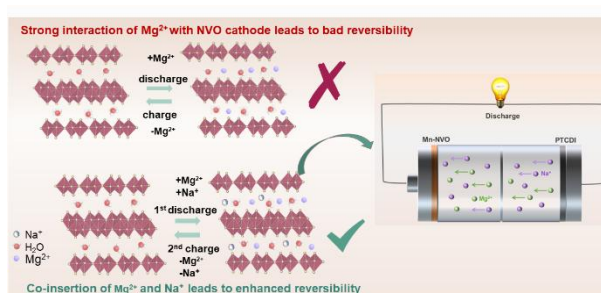
- [42] G. Liang, Z. Gan, X. Wang, X. Jin, B. Xiong, X. Zhang, S. Chen, Y. Wang, H. He, C. Zhi, *ACS Nano* 15 (2021) 17717-17728.
- [43] S. Zheng, D. Shi, D. Yan, Q. Wang, T. Sun, T. Ma, L. Li, D. He, Z. Tao, J. Chen, *Angew. Chem. Int. Ed. Engl.* 61 (2022) e202117511.
- [44] X. Lin, J. Liu, H. Zhang, Y. Zhong, M. Zhu, T. Zhou, X. Qiao, H. Zhang, T. Han, J. Li, *Adv. Energy Mater.* 8 (2021) 2002298.
- [45] X. Wang, H. Dong, A. Eddine Lakraychi, Y. Zhang, X. Yang, H. Zheng, X. Han, X. Shan, C. He, Y. Yao, *Mater. Today* 55 (2022) 29-36.
- [46] H. Chen, H. Qin, L. Chen, J. Wu, Z. Yang, *J. Alloys Compd.* 842 (2020) 155912.
- [47] S. Ding, X. Dai, Y. Tian, B. Song, L. Wang, G. Li, S. Li, J. Huang, Z. Li, A. Meng, *Nano Energy* 93 (2022) 106838.
- [48] X. Qu, A. Du, T. Wang, Q. Kong, G. Chen, Z. Zhang, J. Zhao, X. Liu, X. Zhou, S. Dong, G. Cui, *Angew. Chem. Int. Ed. Engl.* 61 (2022) e202204423.
- [49] R. Zhang, C. Cui, R. Xiao, L. Ruinan, T. Mu, H. Huo, Y. Ma, G. Yin, P. Zuo, *Chem. Eng. J.* 444 (2022) 136592.
- [50] X.-F. Ma, H.-Y. Li, X. Zhu, W. Ren, X. Zhang, J. Diao, B. Xie, G. Huang, J. Wang, F. Pan, *Small* 18 (2022) 2202250.
- [51] K. W. Leong, W. Pan, Y. Wang, S. Luo, X. Zhao, D. Y. C. Leung, *ACS Energy Lett.* 7 (2022) 2657-2666.
- [52] R. Li, J. Yu, F. Chen, Y. Su, K. Chan, Z. Xu, *Adv. Funct. Mater.* 33 (2023) 2214304.
- [53] E. Li, M. Wang, Y. Feng, L. Yang, Q. Li, Z. Yang, J. Chen, B. Yu, B. Guo, Z. Ma, Y. Huang, J. Liu, X. Li, *J. Energy Chem.* 94 (2024) 148-157.
- [54] L. Ma, X. Li, G. Zhang, Z. Huang, C. Han, H. Li, Z. Tang, C. Zhi, *Energy Storage Mater.* 31 (2020) 451-458.
- [55] Y. Jing, Q. Lv, Y. Chen, B. Wang, B. Wu, C. Li, S. Yang, Z. He, D. Wang, H. Liu, S. Dou, *J. Energy Chem.* 94 (2024) 158-168.
- [56] X. Yu, G. Zhao, C. Wu, H. Huang, C. Liu, X. Shen, M. Wang, X. Bai, N. Zhang, *J. Mater. Chem. A* 9 (2021) 23276-23285.

[57] J. Bae, H. Park, X. Guo, X. Zhang, J. H. Warner, G. Yu, Energy Environ. Sci. 14 (2021) 4391-4399.

[58] J. Wang, L. Jiao, Q. Liu, W. Xin, Y. Lei, T. Zhang, L. Yang, D. Shu, S. Yang, K. Li, C. Li, C. Yi, H. Bai, Y. Ma, H. Li, W. Zhang, B. Cheng, J. Energy Chem. 94 (2024) 10-18.

Graphical abstract

This work presents a novel high-performance and high-safe magnesium-sodium hybrid ion batteries (MSHBs) system that has a large potential for future energy storage applications.



Supporting Information

High-performance magnesium/sodium hybrid ion battery based on sodium vanadate oxide for reversible storage of Na⁺ and Mg²⁺

Xiaoke Wang ^{a,b,c}, Titi Li ^b, Xixi Zhang ^b, Yaxin Wang ^c, Hongfei Li ^c, Hai-Feng Li ^{a,*}, Gang Zhao ^{b,*}, Cuiping Han ^{d,*}

^a Joint Key Laboratory of the Ministry of Education, Institute of Applied Physics and Materials Engineering, University of Macau, Avenida da Universidade, Taipa, Macao SAR, 999078, China

^b School of Physics and Technology, University of Jinan, Shandong 250022, PR China

^c Songshan Lake Materials Laboratory, Dongguan, Guangdong, 523808, China

^d Faculty of Materials Science and Energy Engineering / Institute of Technology for Carbon Neutrality, Shenzhen Institute of Advanced Technology, Chinese Academy of Sciences, Shenzhen, Guangdong, 518055, China

* Corresponding authors.

E-mail addresses: haifengli@um.edu.mo (H. Li), sps_zhaog@ujn.edu.cn (G. Zhao), cp.han@siat.ac.cn (C.P. Han).

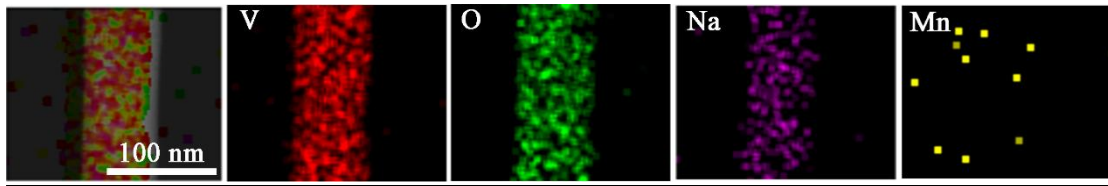


Fig. S1. Corresponding TEM-EDS elemental mappings of Mn-NVO, including V, O, Na and Mn.

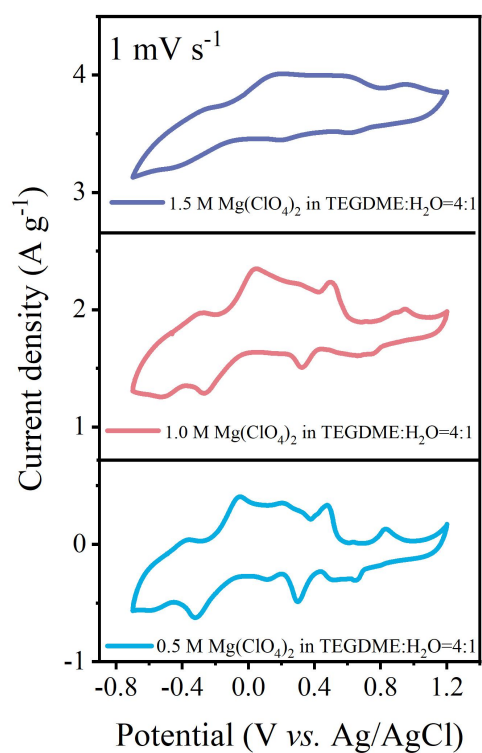


Fig. S2. CV of Mn-NVO cathode in various concentrations Mg(ClO₄)₂ of electrolyte.

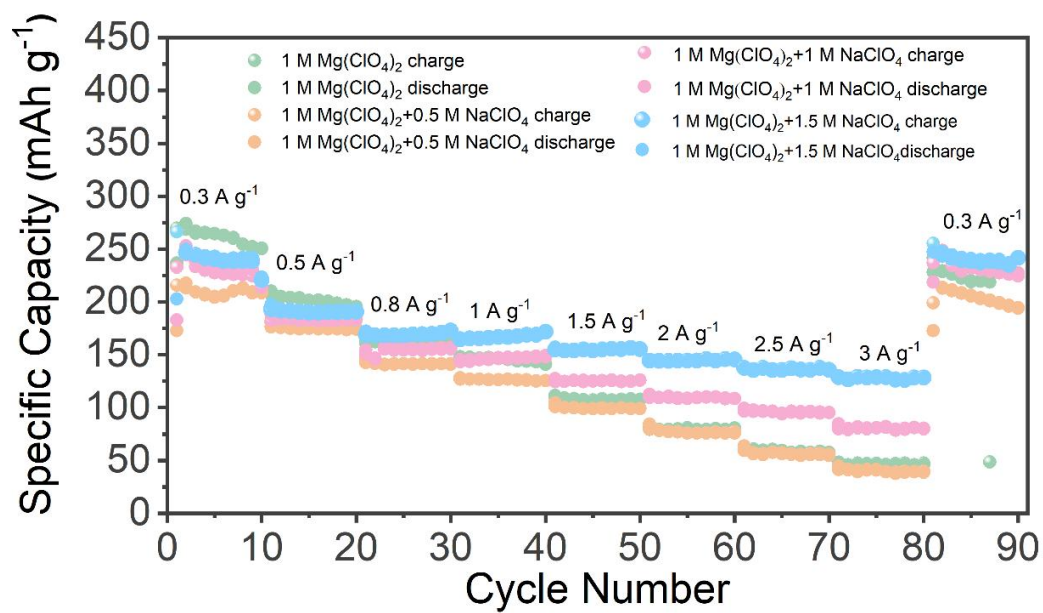


Fig. S3. Rate performance of Mn-NVO cathode in different amounts of sodium salts with 0.5 M, 1.0 M, and 1.5 M NaClO₄.

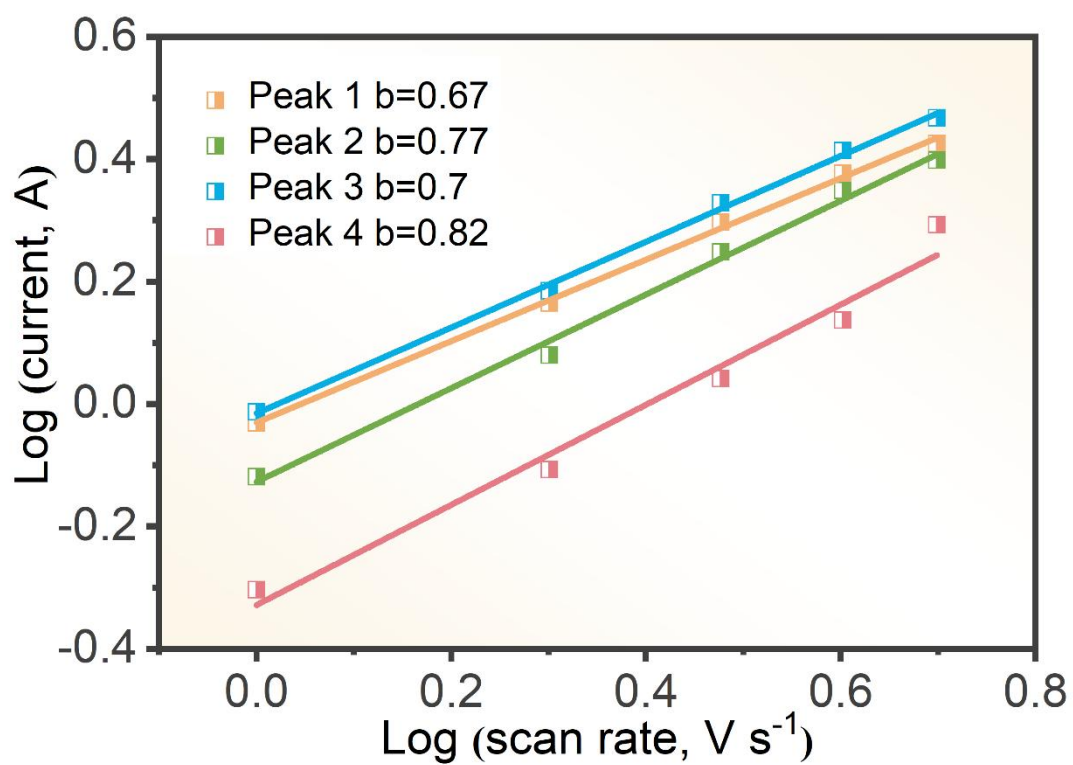
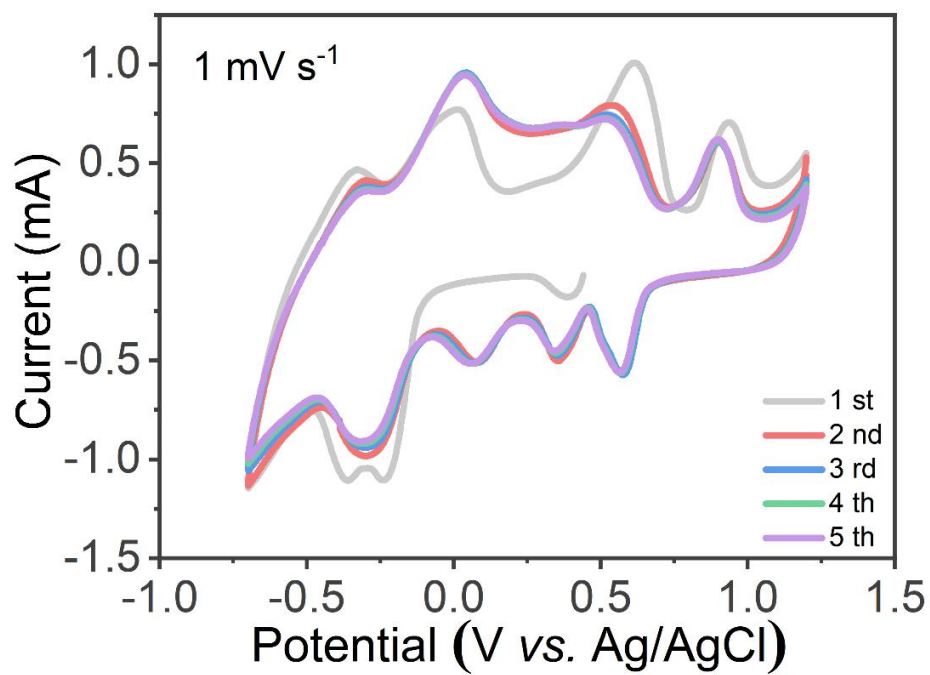


Fig. S4. $\log(\text{current})$ versus $\log(\text{scan rate})$ and corresponding b -values.



Fi

g. S5. Cyclic voltammetry (CV) curves of Mn-NVO cathode in MSHBs at the scan rate of 1 mV s⁻¹.

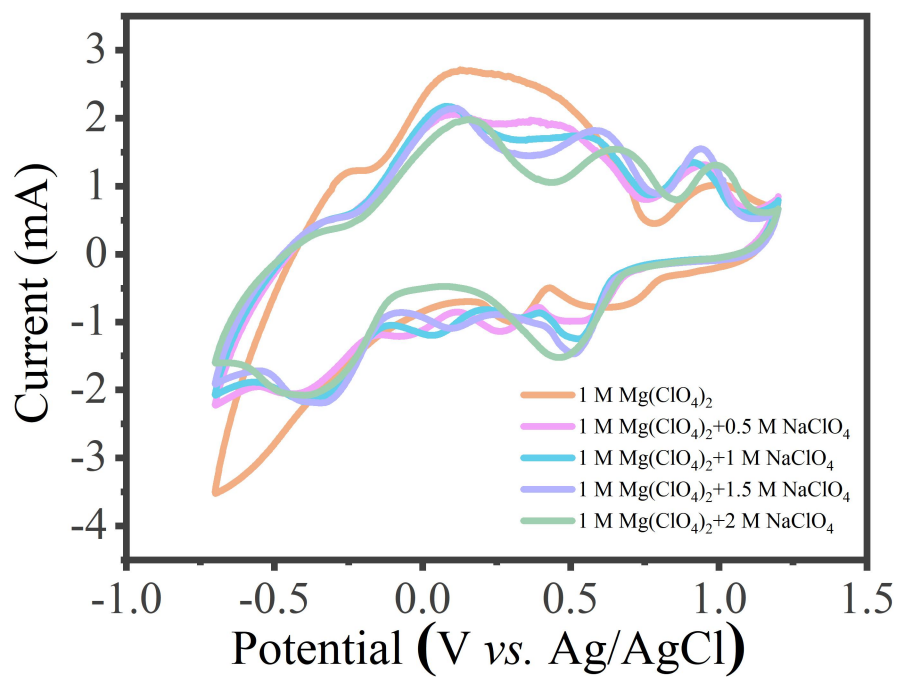


Fig. S6. CV of Mn-NVO cathode (within -0.7-1.2 V) after the addition of different proportions of sodium salts in MIBs.

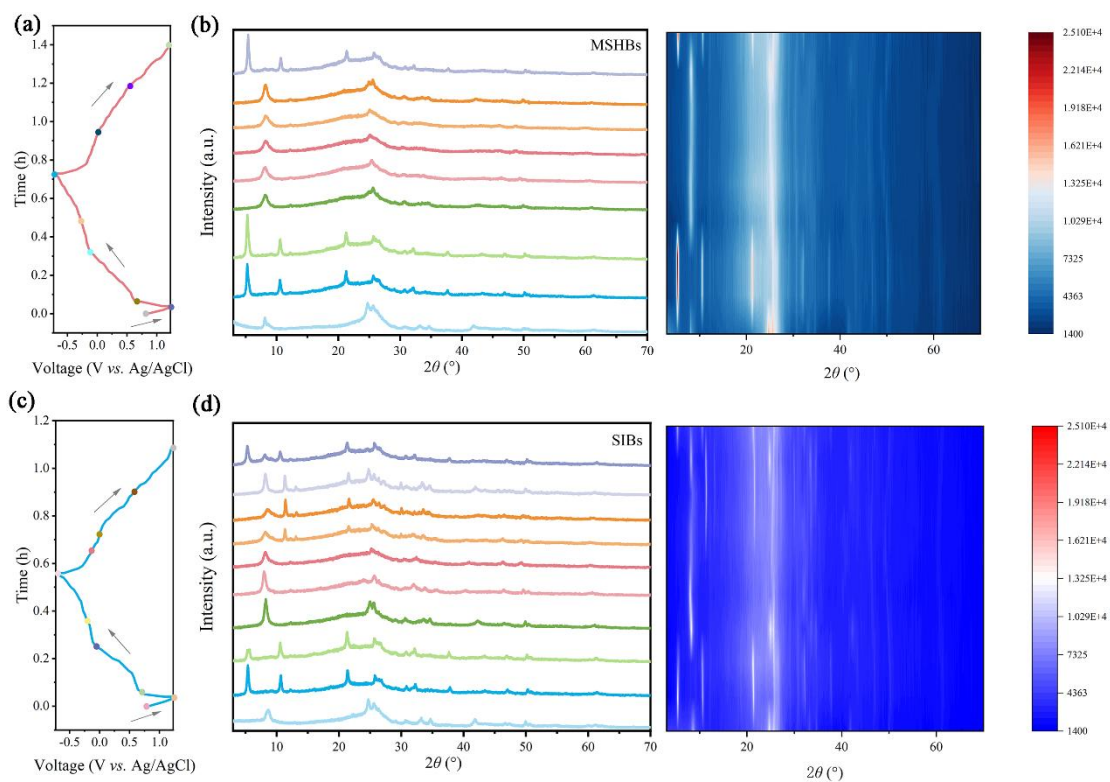


Fig. S7. (a) The initial voltage-time curves of Mn-NVO cathode in MIBs (0.2 A g⁻¹); (b) corresponding *ex-situ* XRD patterns of the Mn-NVO cathode taken at the indicated points in (a); (c) The initial voltage-time profiles of Mn-NVO cathode in MSHBs (0.2 A g⁻¹); (d) Corresponding *ex-situ* XRD patterns of the Mn-NVO cathode taken at the indicated points in (c).

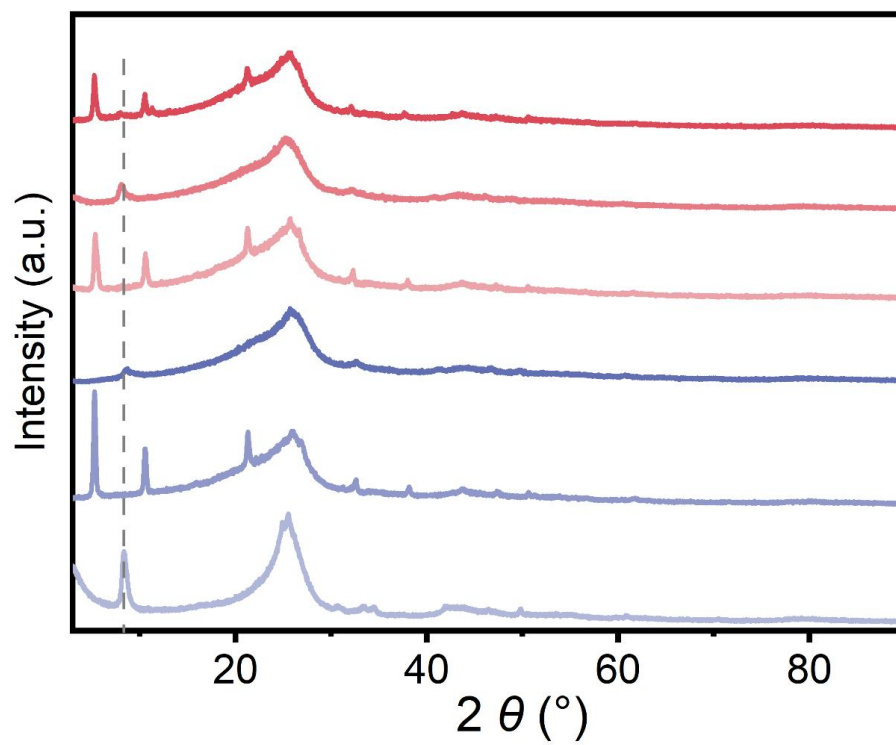


Fig. S8. The *ex-situ* XRD patterns of the Mn-NVO cathode in SIBs at 0.2 A g^{-1} .

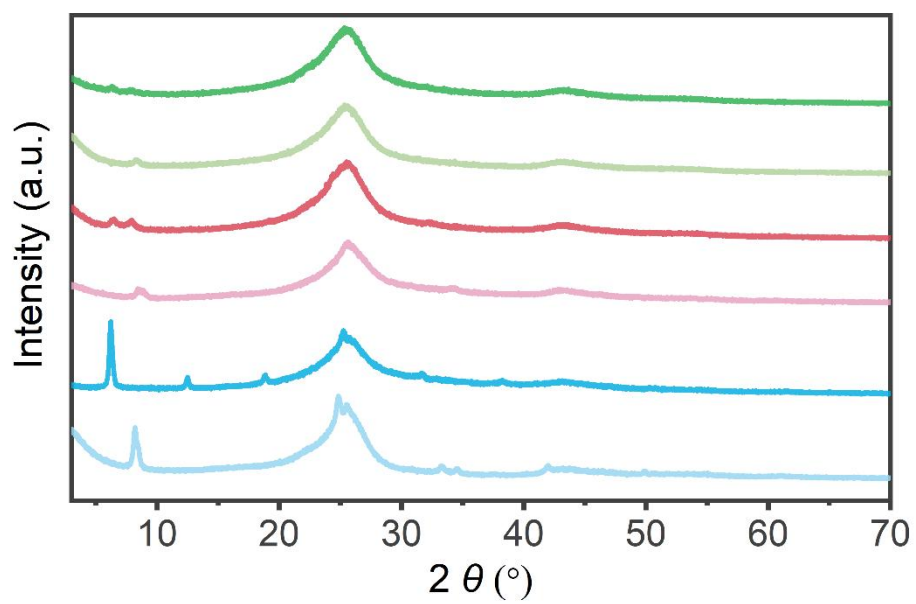


Fig. S9. The *ex-situ* XRD patterns of the Mn-NVO cathode with 1 M Mg $(\text{ClO}_4)_2 \cdot 6\text{H}_2\text{O}$ + 1.5 M NaClO₄ in H₂O at 0.2 A g⁻¹.

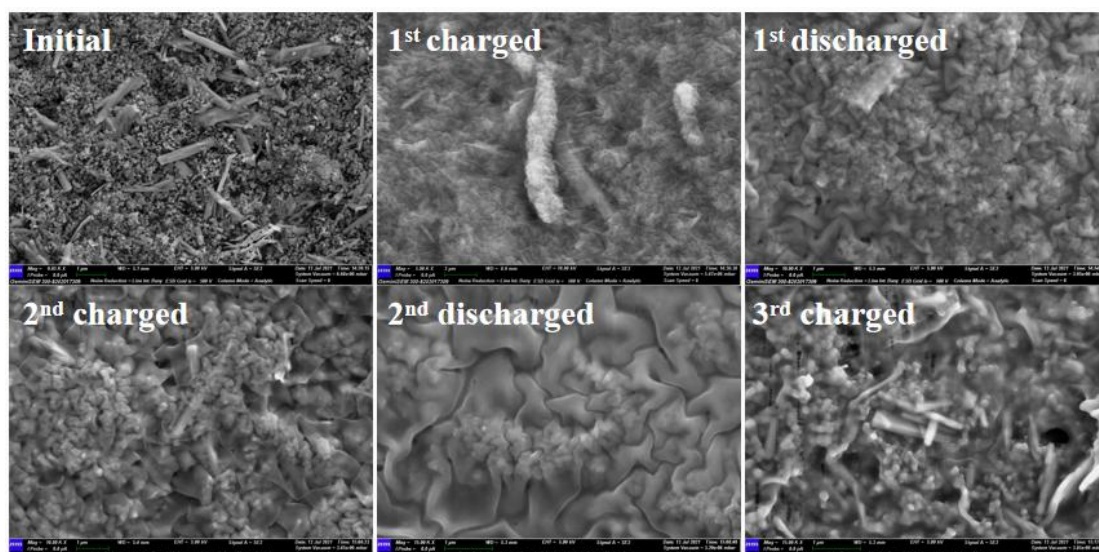


Fig. S10. (a) The SEM images of Mn-NVO cathode and at different states (initial, 1st charged, 1st discharged, 2nd charged, 2nd discharged, and 3rd charged state) in MSHBs, respectively.

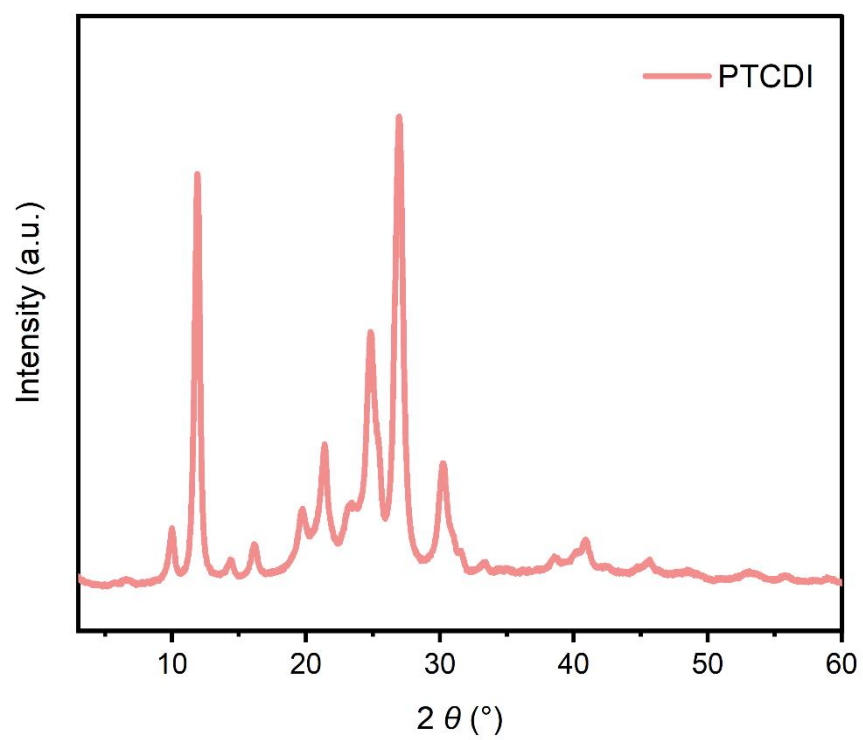


Fig. S11. XRD of the PTCDI, where the PTCDI is well crystallized.

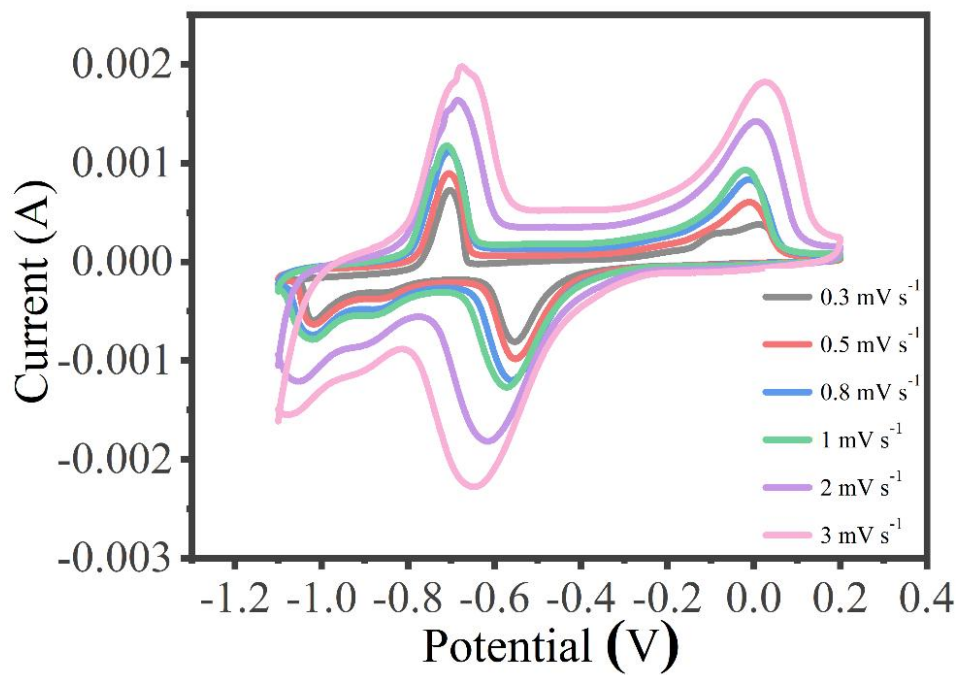


Fig. S12. CV of PTCDI anode (within -1.1-0.2 V) in different scan rates of 0.3, 0.5, 0.8, 1.0, 2.0, and 3.0 mV s⁻¹ in SIBs.

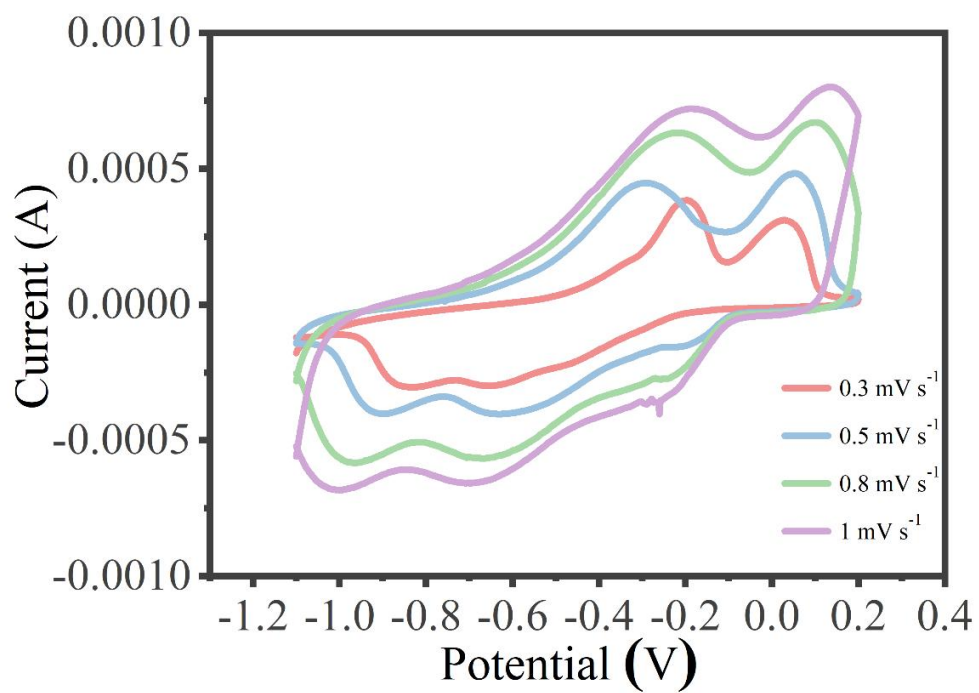


Fig. S13. CV of PTCDI anode (within -1.1-0.2 V) in different scan rates of 0.3, 0.5, 0.8, and 1.0 mV s⁻¹ in MIBs.

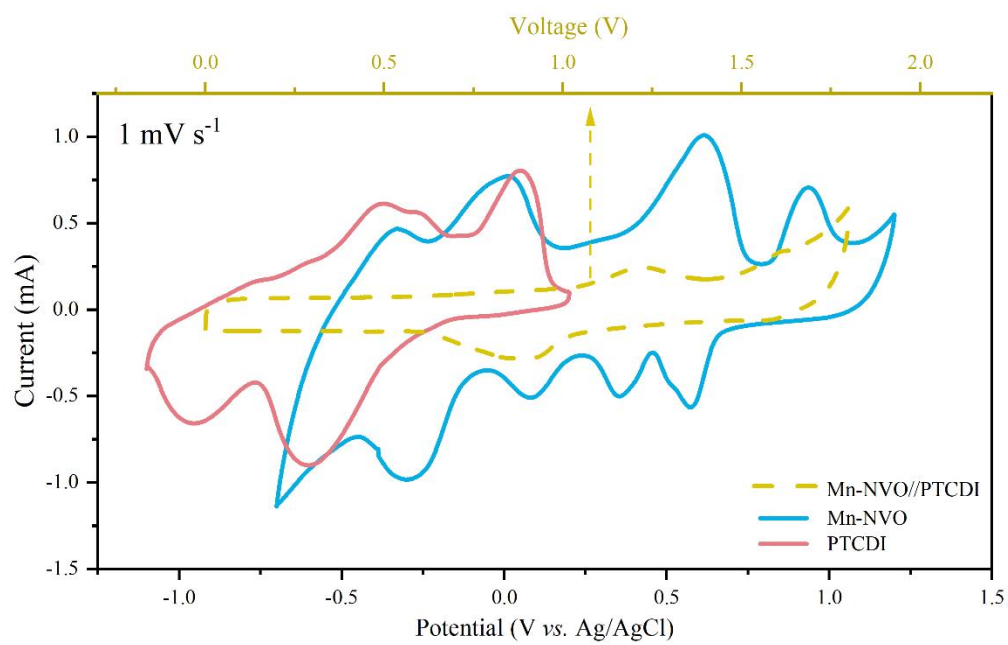


Fig. S14. CV curves of Mn- NVO, PTCDI and the full battery.

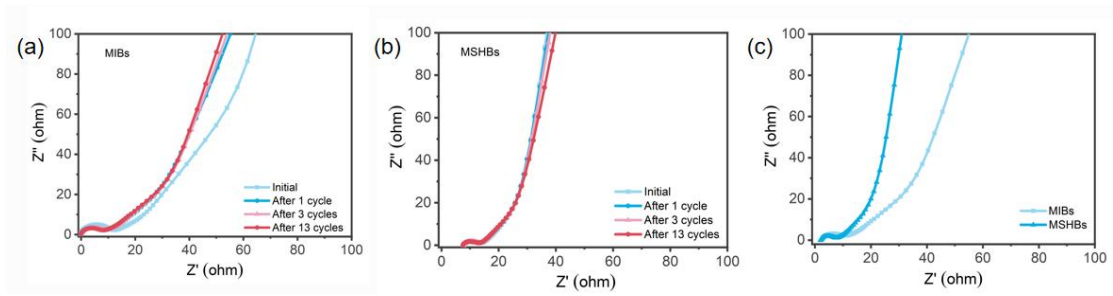


Fig. S15. (a-c) The EIS spectra of the Mn-NVO//PTCDI coin batteries using the Mg^{2+} electrolytes and the mixed Mg^{2+}/Na^{+} electrolytes at various cycling numbers, respectively.

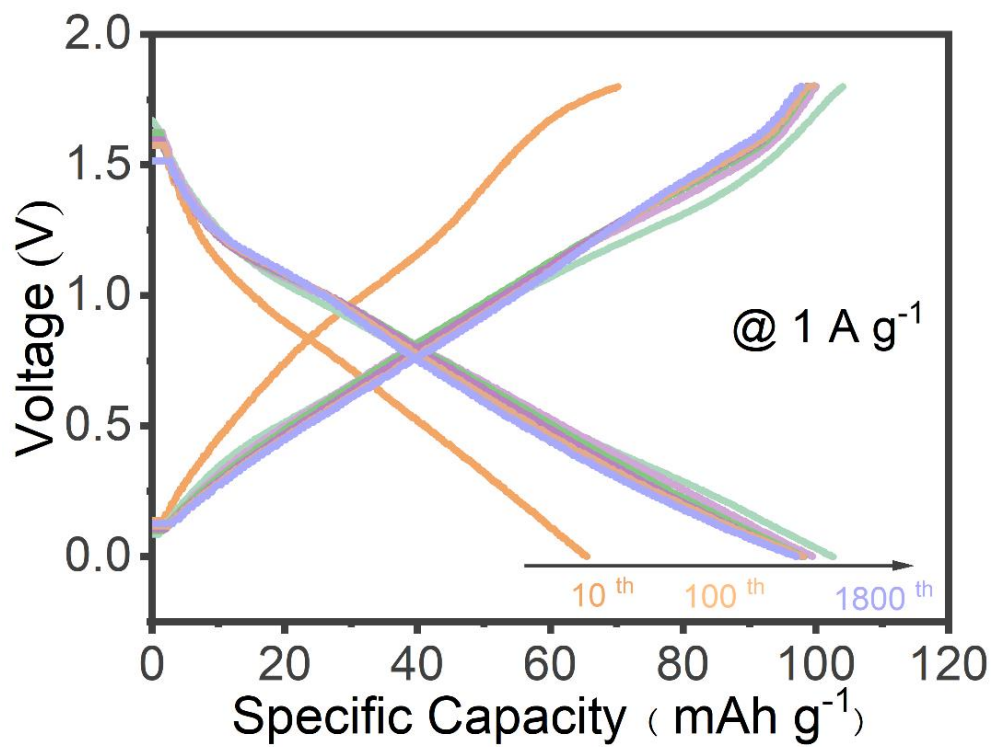


Fig. S16. Charge–discharge voltage profiles of Mn-NVO//PTCDI full MSHBs after different cycles.

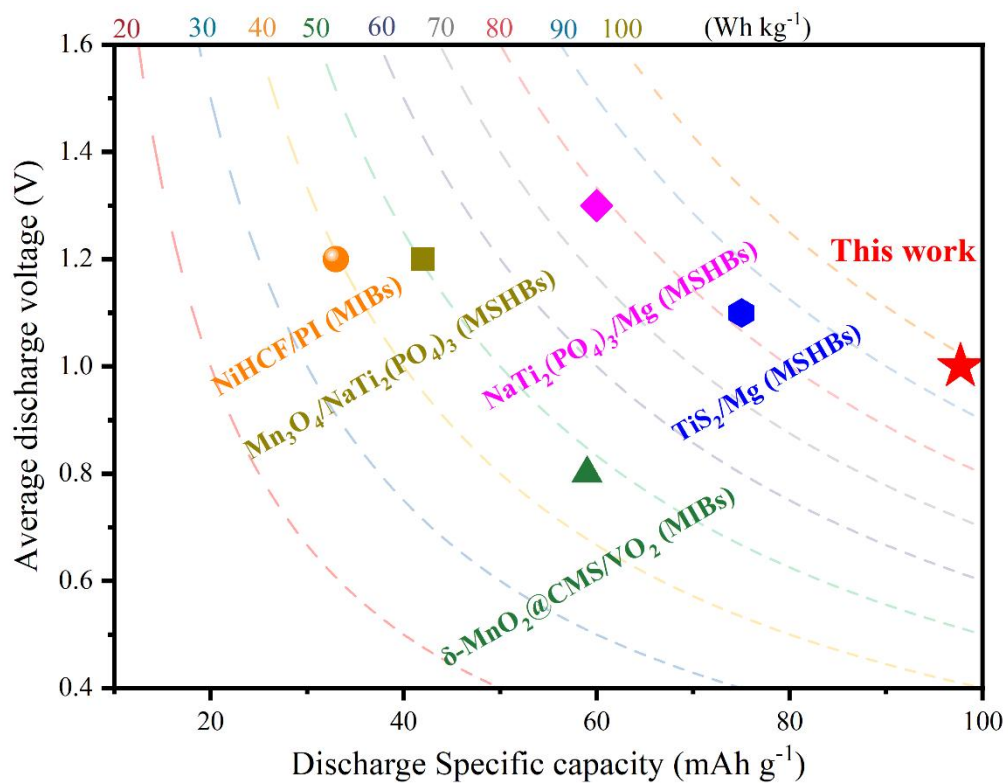


Fig. S17. Performance comparison with other rechargeable Mg based batteries.

Table S1. Performance comparison of Mn-NVO with reported cathode materials for MNHBs.

Cathode materials	Anode materials	Electrolyte (Mg salt/Na salt (solvent))	Capacity retention/Cycle number/current	Ref.
Mn- NVO	PTCDI	Mg (ClO₄)₂ /NaClO₄ (TEGDME/H₂O=4:1)	~104 mAh g⁻¹ /10000/1000 mA g⁻¹	This work
FeS₂	Mg	Mg (BH ₄) ₂ /NaBH ₄ (DGM)	225 mAh g ⁻¹ /40 /200 mA g ⁻¹	[1]
Na₂VTi (PO₄)₃	Mg	Mg (HMDS) ₂ -AlCl ₃ /NaTFSI (DGM)	~90 mAh g ⁻¹ /1000/500 mA g ⁻¹	[2]
Mn₃O₄	NaTi ₂ (PO ₄) ₃	MgSO ₄ /Na ₂ SO ₄ (H ₂ O)	~65 mAh g ⁻¹ /6000 /1000 mA g ⁻¹	[3]
Mg_{1.5}VCr (PO₄)₃	FeVO ₄	Mg (ClO ₄) ₂ /NaClO ₄ (AN/H ₂ O=4:1)	104.7 mAh g ⁻¹ /1350/1000 mA g ⁻¹	[4]
FeFe (CN)₆	Mg	[Mg ₂ (μ-Cl) ₂] [AlCl ₄] ₂ /NaAlCl ₄ (DME)	~117 mAh g ⁻¹ /50/140 mA g ⁻¹	[5]

Table S2. Elemental content of Mn-NVO cathode in MSHBs with XPS depth profiling after 140 s of C 1s, V 2p, O 1s, F 1s, Na 1s, and Mg 1s in initial, the first fully charged, the first fully discharged, the second fully charged, the second fully discharged states, and the third fully charged.

	initial	1 st charged	1 st discharged	2 nd charged	2 nd discharged	3 rd charged
Na	1.04 %	1.81 %	1.18 %	1.6 %	1.62 %	1.34 %
Mg	0	16.65%	21.1 %	15.67 %	19.36 %	6.83 %

Table S3. The TEM-EDS results in MSHBs in initial, first fully charged, first fully discharged, second fully charged, and second fully discharged states.

TEM-EDS	initial	1 st charged	1 st discharged	2 nd charged
Na	5.62 %	0.84 %	1.3 %	1.27 %
Mg	0	1.55 %	2.6 %	1.04 %

Table S4. Performance comparison of various Mg based batteries reported to date.

Battery type	Electrodes	Average discharge voltage per current (V @ A g ⁻¹)	Specific capacity per current (mAh g ⁻¹ @ A g ⁻¹)	Energy density per current (Wh kg ⁻¹ @ A g ⁻¹)	Ref.
MSHBs	Mn- NVO/PTCDI	1 @ 0.1	97.7 @ 0.1^{a)}	97.7 @ 0.1^{a)}	This work
MSHBs	Mn ₃ O ₄ /NaTi ₂ (PO ₄) ₃	1.2	42 @ 5	50.4 @ 5	[3]
MSHBs	TiS ₂ /Mg	1.1	75 @ 4	82.5 @ 4	[6]
MSHBs	NaTi ₂ (PO ₄) ₃ /Mg	1.4	60 @ 1.3	84 @ 1.3	[7]
MIBs	NiHCF/PI	1.2 @ 1	33 @ 1	40 @ 1	[8]
MIBs	δ-MnO ₂ @CMS/VO ₂	0.8 @ 0.5	59 @ 0.5	47 @ 0.5	[9]

a) Discharge capacities and energy densities are reported per mass of active material at the cathode.

References

- [1] M. Walter, K. V. Kravchyk, M. Ibáñez, M. V. Kovalenko, *Chem. Mater.* 2015, 27, 7452.
- [2] Y. Zhang, J. Gui, T. Li, Z. Chen, S.-a. Cao, F. Xu, *Chemical Engineering Journal* 2020, 399, 125689.
- [3] X. Cao, L. Wang, J. Chen, J. Zheng, *Journal of Materials Chemistry A* 2018, 6, 15762.
- [4] Y. Tang, X. Li, H. Lv, W. Wang, Q. Yang, C. Zhi, H. Li, *Angewandte Chemie International Edition* 2021, 60, 5443.
- [5] H. Dong, Y. Li, Y. Liang, G. Li, C.-J. Sun, Y. Ren, Y. Lu, Y. Yao, *Chem. Commun.* 2016, 52, 8263.
- [6] X. Bian, Y. Gao, Q. Fu, S. Indris, Y. Ju, Y. Meng, F. Du, N. Bramnik, H. Ehrenberg, Y. Wei, *Journal of Materials Chemistry A* 2017, 5, 600 – 608.
- [7] Y. Xu, W. Cao, Y. Yin, J. Sheng, Q. An, Q. Wei, W. Yang, L. Mai, *Nano Energy* 2019, 55, 526–533.
- [8] L. Chen, J. Bao, X. Dong, D. Truhlar, Y. Wang, C. Wang, Y. Xia, *ACS Energy Lett.* 2017, 2, 1115–1121.
- [9] S. Liu, R. Zhang, J. Mao, Y. Zhao, Q. Cai, Z. Guo, *Science Advances* 2022, 8, eabn5097.